

advances.sciencemag.org/cgi/content/full/7/20/eabd5835/DC1

Supplementary Materials for

An inverse-breathing encapsulation system for cell delivery

Long-Hai Wang, Alexander Ulrich Ernst, James Arthur Flanders, Wanjun Liu, Xi Wang, Ashim K. Datta, Boris Epel, Mrignayani Kotecha, Klearchos K. Papas, Minglin Ma*

*Corresponding author. Email: mm826@cornell.edu

Published 14 May 2021, *Sci. Adv.* **7**, eabd5835 (2021)
DOI: [10.1126/sciadv.abd5835](https://doi.org/10.1126/sciadv.abd5835)

The PDF file includes:

Figs. S1 to S32
Table S1
Legends for movies S1 to S3

Other Supplementary Material for this manuscript includes the following:

(available at advances.sciencemag.org/cgi/content/full/7/20/eabd5835/DC1)

Movies S1 to S3

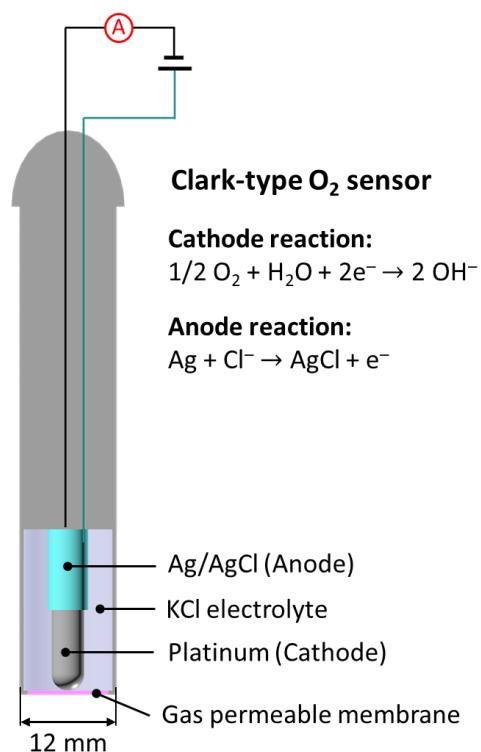


Fig. S1. Clark-type O₂ sensor. Schematic illustrating the components of a Clark-type O₂ sensor (Vernier). O₂ diffuses through a gas permeable membrane to an O₂-reducing cathode, which is polarized against an internal Ag/AgCl anode. pO₂ is linearly proportional to the detected current strength.

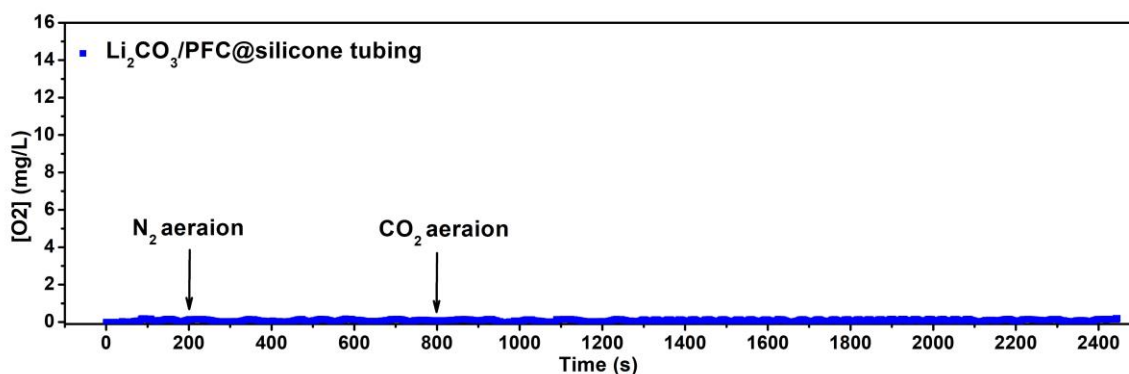


Fig. S2. No CO₂ responsiveness in the control Li₂CO₃/PFC@silicone tubing. O₂ concentration recordings of the sensor (Vernier) submerged near the control sample during N₂ and CO₂ aeration.

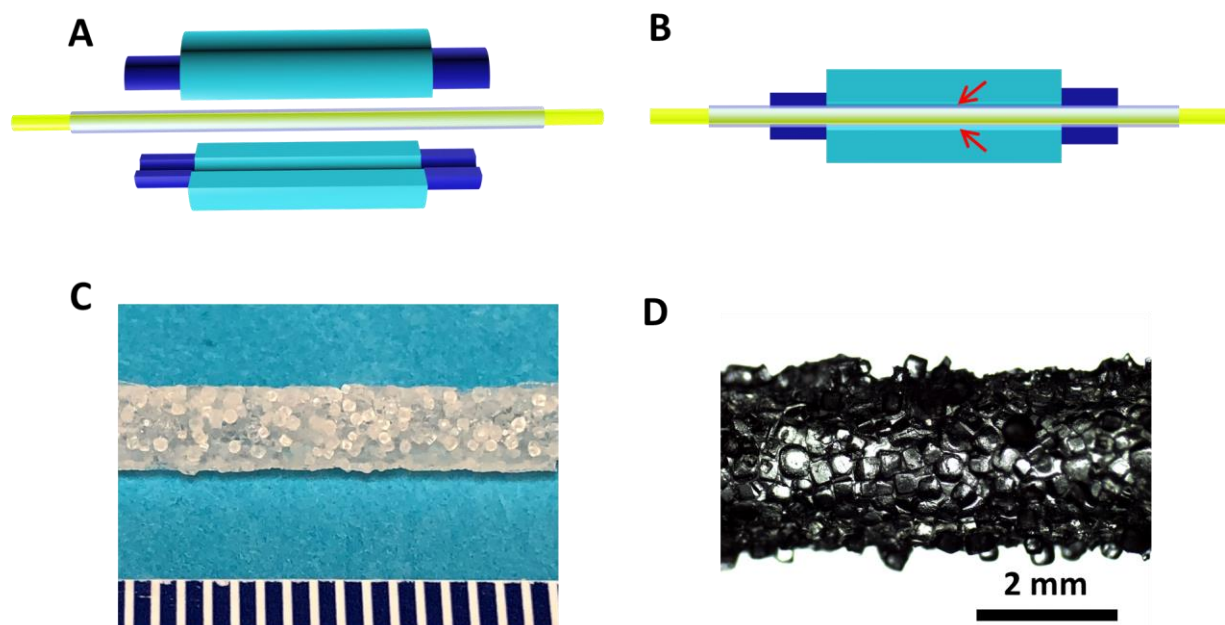


Fig. S3. The salt leaching method. (A) Schematic representing a two-part hollow mold for silicone tubing surface roughness modification. (B) Schematic showing the gap (red arrows) between the tubing and hollow mold used to control the coating thickness, and a solid rod (yellow) used to keep the tubing straight inside the mold. (C) Digital and (D) stereo microscope images of the NaCl/PDMS modified surface before leaching. Photo credit (C): Long-Hai Wang, Cornell University.

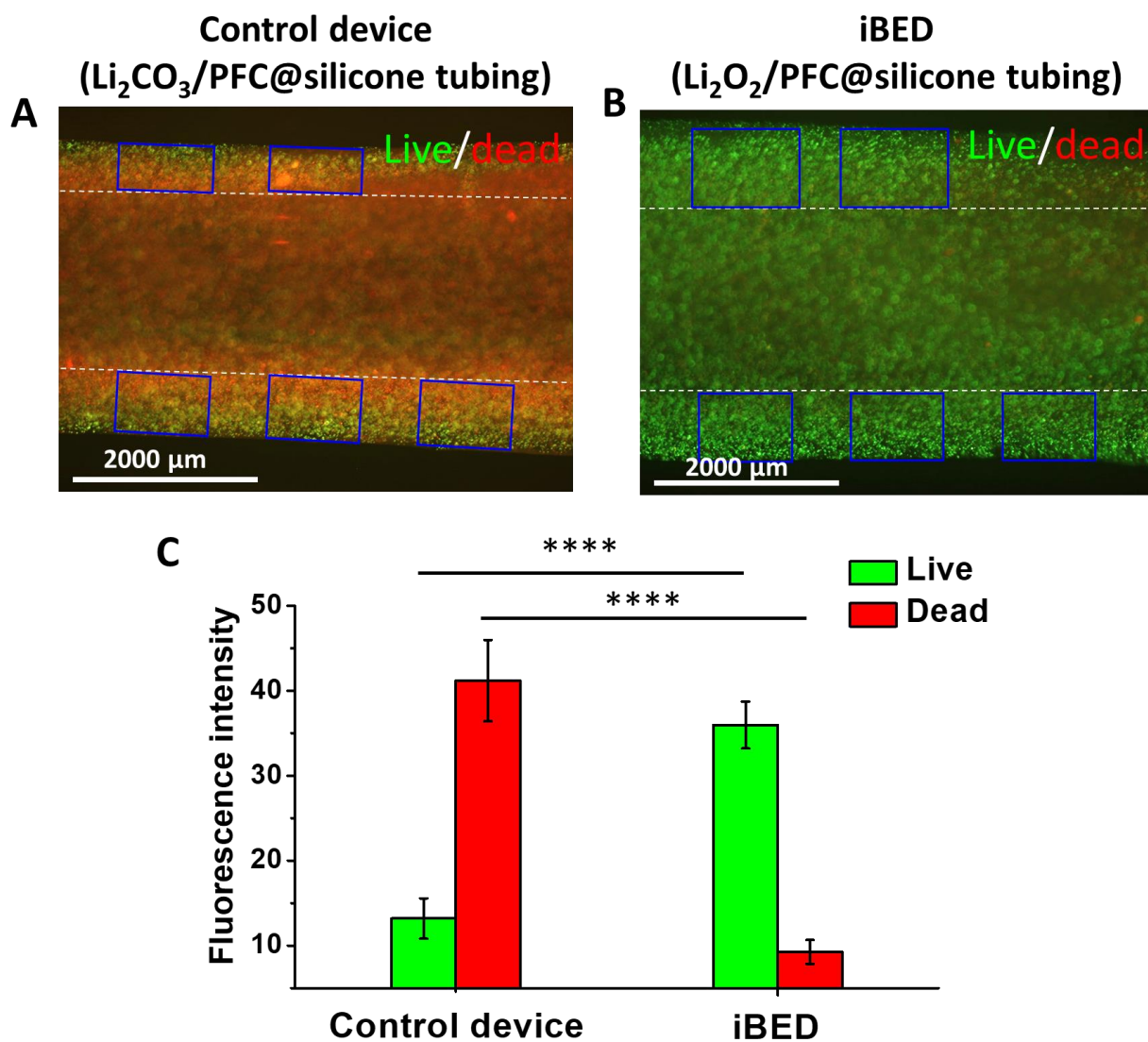


Fig. S4. Viability of encapsulated cells under hypoxic incubation. (A and B) Fluorescent microscopy images of INS-1 cells stained for viability (alive = green, dead = red) following 24-h culture in 1% O_2 , 5% CO_2 in (A) $\text{Li}_2\text{CO}_3/\text{PFC}$ -containing control device and (B) $\text{Li}_2\text{O}_2/\text{PFC}$ -containing device (iBED). (C) Quantification of the fluorescence intensity of the live-staining and dead-staining cells in the selected regions (blue boxes) of the control device and the iBED. Note, the silicone tubing in the device is indicated by the white dashed lines. The iBED yielded a 2.7-fold improvement in cell viability in comparison to the control device (two-way ANOVA followed by Tukey's post-hoc p -value adjustment, **** $p < 0.0001$), quantitatively confirming the ability of iBED to improve cell survival in hypoxic conditions.

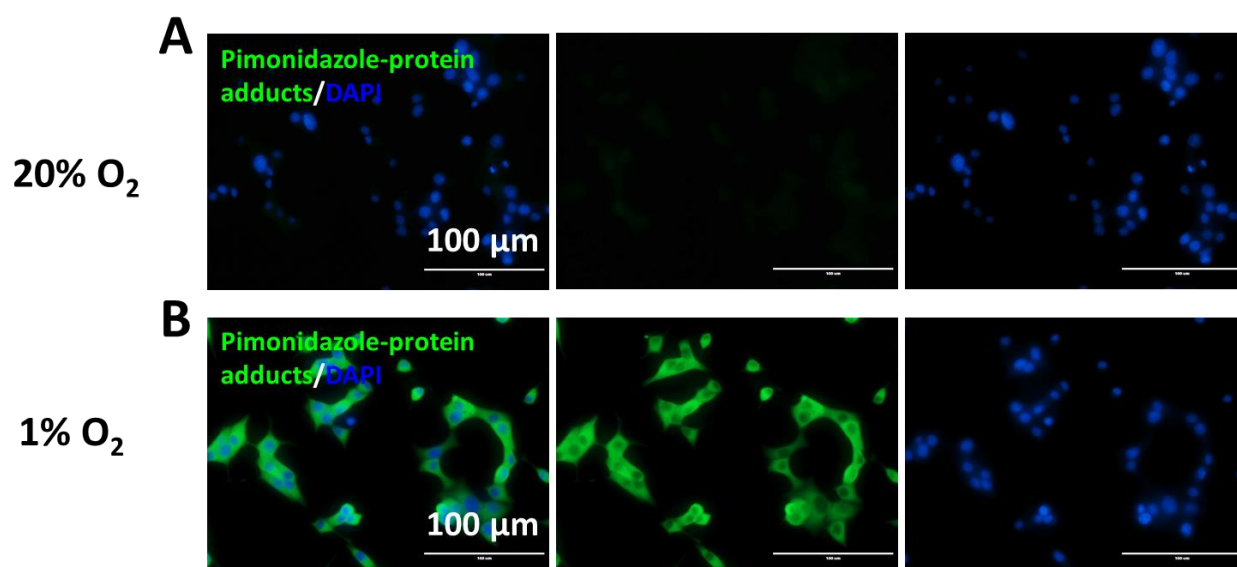


Fig. S5. Pre-experiment of pimonidazole as a hypoxia marker in INS-1 cells. Pimonidazole-protein adducts (green) and nuclei (DAPI; blue) staining of INS-1 cells (50 k cells per well in a 48-well plate) incubated in (A) a normal incubator (~20% O₂, 5% CO₂) and (B) a hypoxia incubator (1% O₂, 5% CO₂) for 24 h.

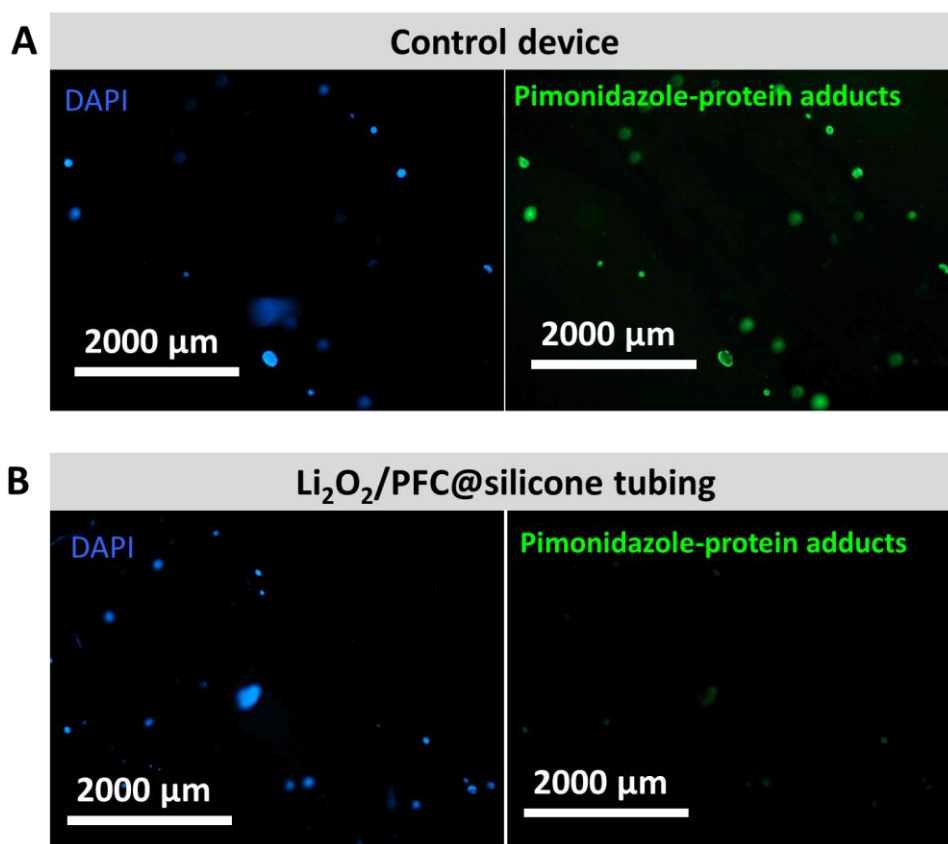


Fig. S6. Staining of islet hypoxia. Microscope images of staining of nuclei (DAPI; blue) and pimonidazole-protein adducts (green) following 24-h culture in 1% O₂, 5% CO₂ of islets in (A) a Li₂CO₃/PFC@silicone control and (B) a Li₂O₂/PFC@silicone construct. (Images in A are separated channels from the merged image in Fig. 2D, and images in B are separated channels from the merged image in Fig. 2E.)

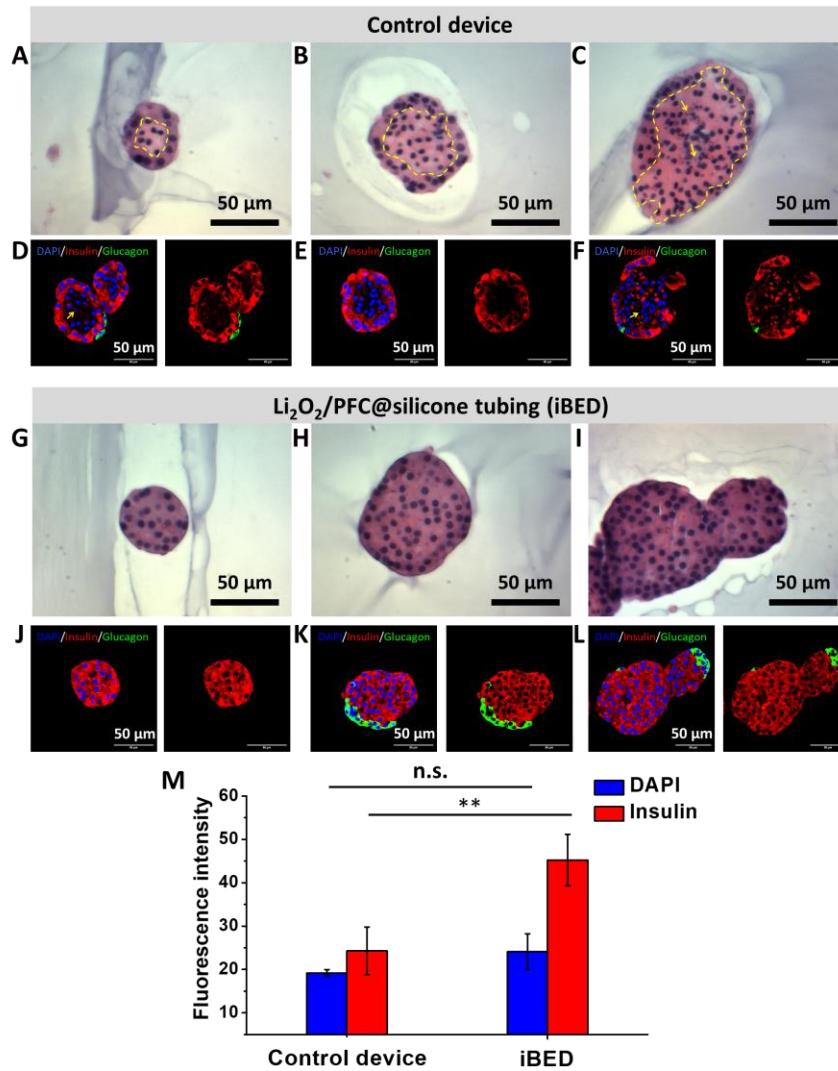


Fig. S7. Morphology and immunohistochemistry of islets after hypoxic incubation. Rat islets encapsulated in (A to F) Li₂CO₃/PFC@silicone controls and (G to L) Li₂O₂/PFC@silicone constructs (iBED) incubated at 1% O₂, 5% CO₂ for 24 h. (A to C) H&E staining of islets in control samples showed a corona of healthy cells, whereas cells in the islet core exhibited pyknosis (cells circumscribed in the dashed yellow line) and nuclear fragmentation (yellow arrows). (D to F) Nuclei (DAPI; blue)/insulin (red)/glucagon (green) immunostaining was positive for insulin and glucagon in the islet periphery but negative in the islet core. (G to I) H&E staining of islets in Li₂O₂/PFC@silicone samples showed round morphologies no indicators of hypoxia. (J to L) Nuclei (DAPI; blue)/insulin (red)/glucagon (green) immunostaining showed islets were intact and positive for insulin throughout and glucagon in peripheral cells, suggesting maintained function. (M) Comparison of islet function in the control device and the iBED by quantification of insulin and DAPI fluorescence intensity of the stained islets to evaluate the islet functionality and pyknosis (shrunken and dark nuclei)/karyorrhexis (fragmented nuclei) in islets, respectively. Specially, islets in the control devices showed a 1.86-fold reduction (two-way ANOVA followed by Tukey's post-hoc *p*-value adjustment, ***p* < 0.01) of insulin expression due to the non-insulin secretion cells in the hypoxic core and 1.25-fold reduction in DAPI content (two-way ANOVA followed by Tukey's post-hoc *p*-value adjustment, n.s., *p* > 0.05) because of the shrunken or fragmented nuclei (though this was not found to be statistically significant) compared to islets in the iBED devices.

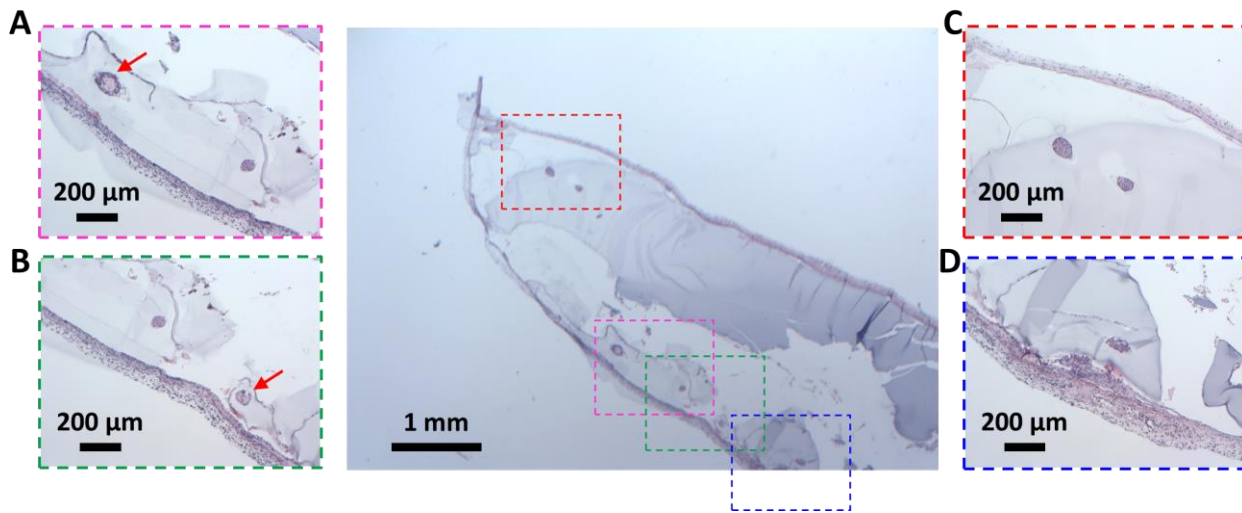


Fig. S8. $\text{Li}_2\text{O}_2/\text{PFC}@\text{silicone}$ construct retrieved from SC rat-to-mouse transplantation. H&E staining of rat islet encapsulated $\text{Li}_2\text{O}_2/\text{PFC}@\text{silicone}$ construct retrieved from mice at 4 weeks. (A to D) Peripheral high magnification images show both healthy islets and unhealthy islets (red arrows).

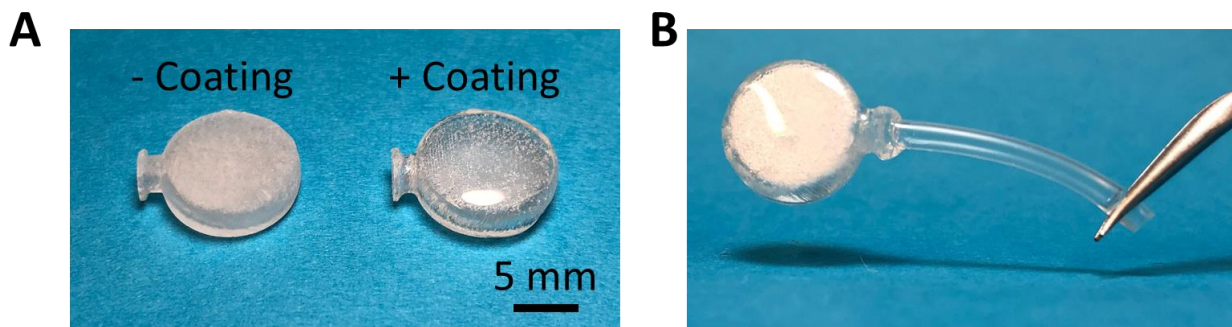


Fig. S9. iBEDv1 components. (A) Digital image showing 3D-printed terminal tank before (left) and after (right) coating with additional resin. (B) Digital image showing the silicone tubing (surface unmodified) attached to the $\text{Li}_2\text{O}_2/\text{PFC}$ -filled terminal tank via a PDMS adapter. Photo credits (A and B): Long-Hai Wang, Cornell University.

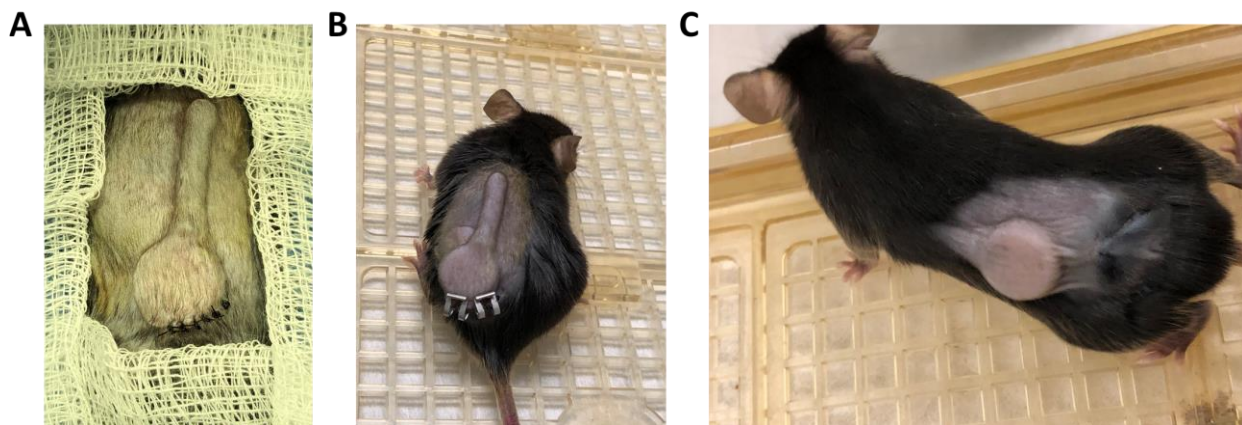


Fig. S10. SC implantation of iBEDv1 in mice. Digital images showing a mouse with a dorsolateral SC transplanted iBEDv1 (A and B) directly after surgery and (C) two weeks post-surgery. Photo credits (A to C): Long-Hai Wang, Cornell University.

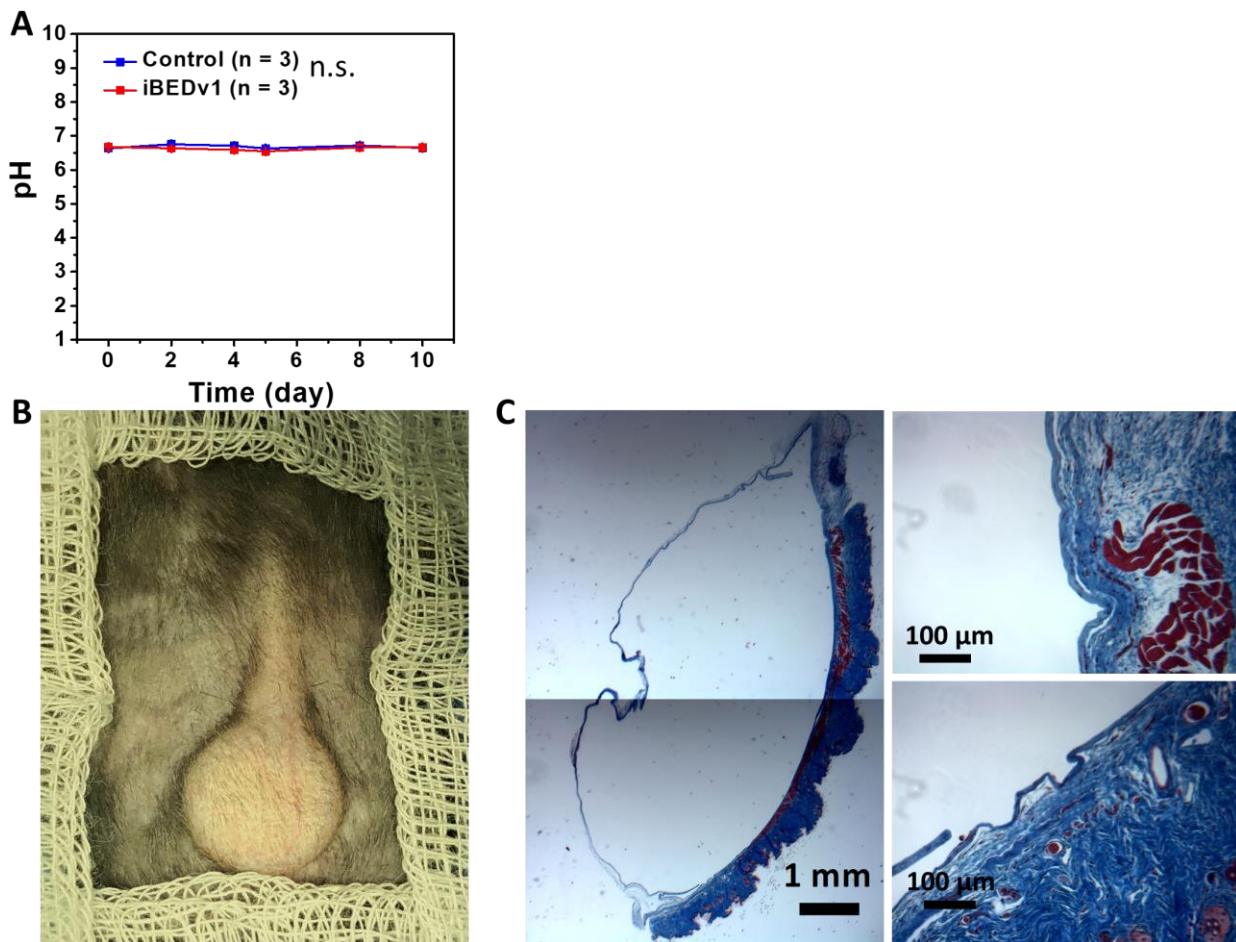


Fig. S11. Biocompatibility of the iBEDv1 and the terminal tank. (A) pH monitoring of saline solution cultured with iBEDv1 devices over 10 days. Normal untreated saline solution was used as the control. No significant pH change was observed, and no statistically significant difference compared with the control (one-way ANCOVA, n.s., $p > 0.05$). (B) Digital image showing the dorsolateral SC transplantation of iBEDv1 in mice emphasizing the terminal tank. (C) Masson's trichrome images of the tissue surrounding the terminal tank following device retrieval at 2 months, showing no indications of an adverse reaction. Photo credit (B): Long-Hai Wang, Cornell University.

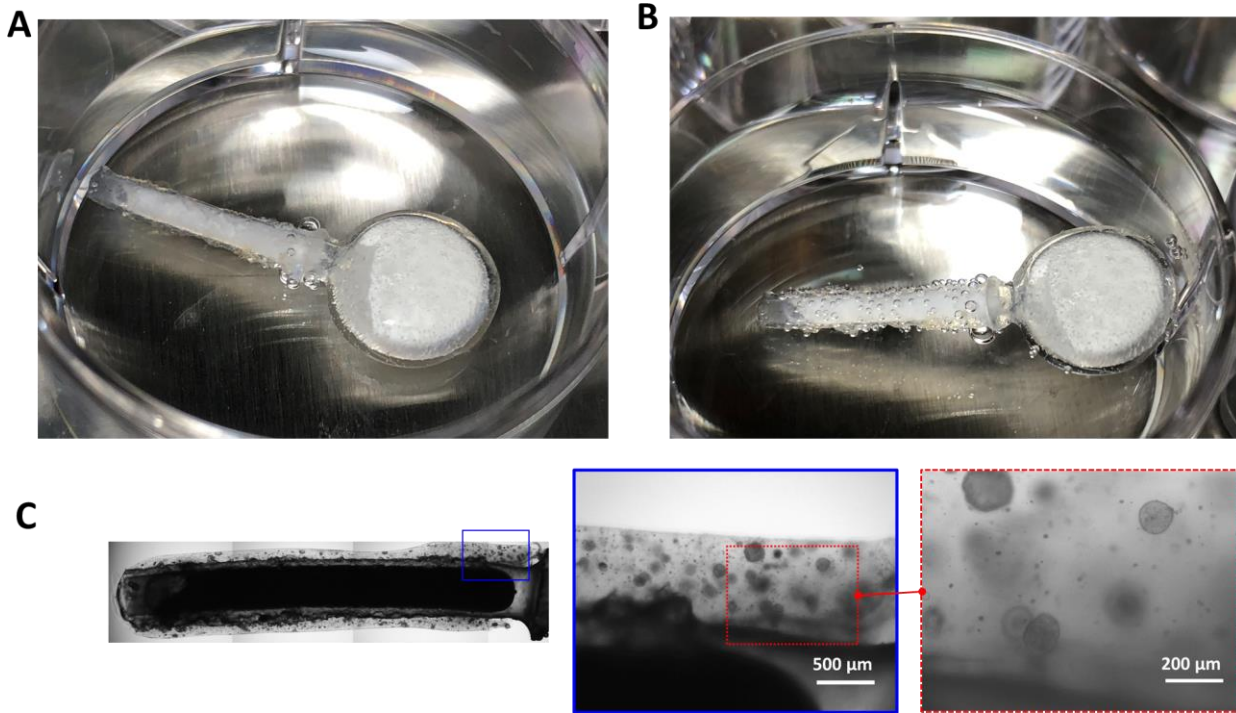


Fig. S12. Maintained CO₂ responsiveness and islet morphology in a retrieved iBEDv1. (A and B) Digital images at two time points of a rat islet encapsulating iBEDv1 retrieved at 2 months from a mouse, incubated at 5% CO₂, 5% O₂ (note, the cell encapsulation hydrogel was stripped prior to incubation). Bubbles, indicating active CO₂-responsive O₂ production, formed (A) near the terminal tank first, and (B) eventually along the tubing lumen, suggesting a z-gradient of O₂. (C) Microscope images of the encapsulated islets, showing round and well-defined islet morphology in regions near the tank. Photo credits (A and B): Long-Hai Wang, Cornell University.

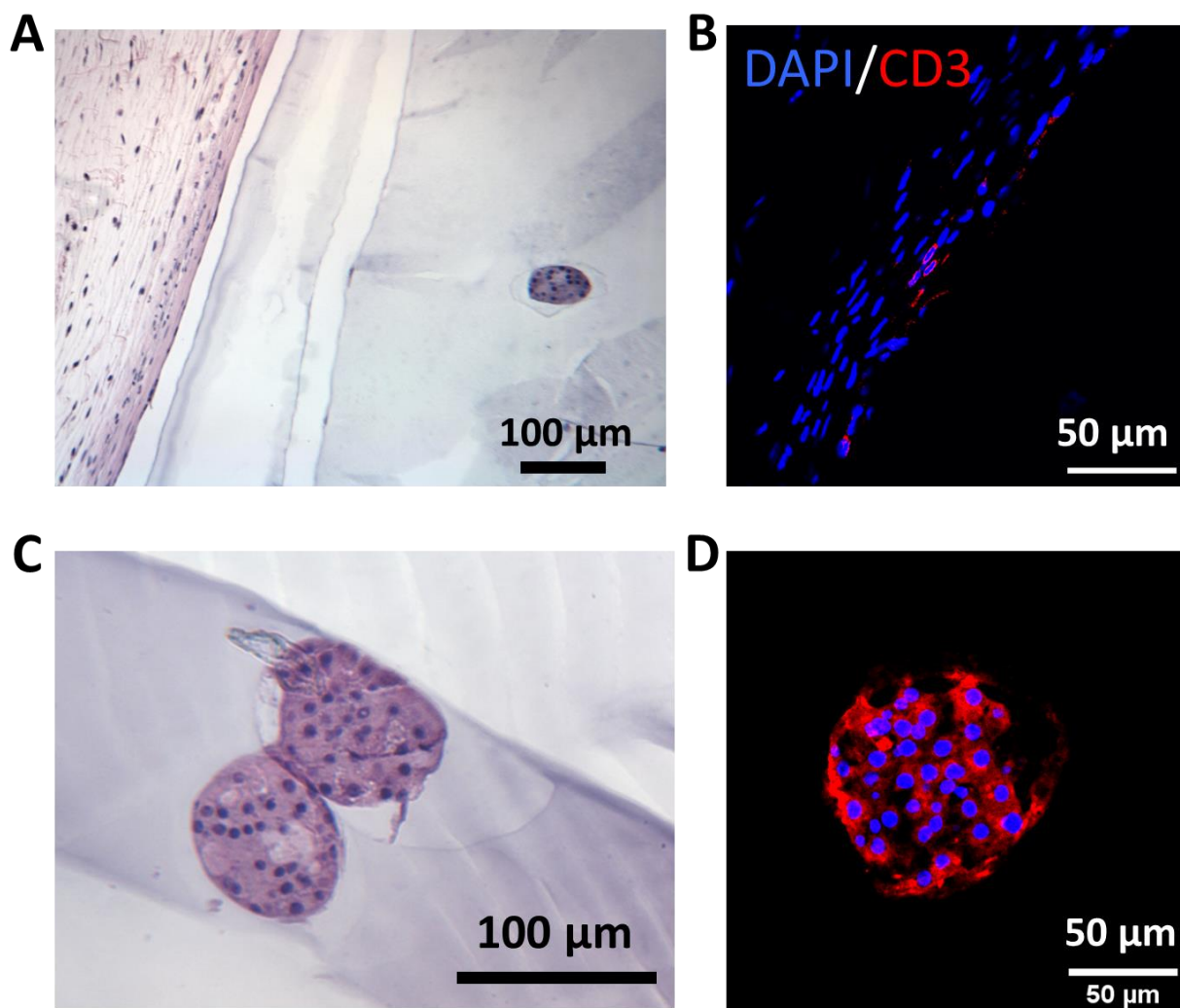


Fig. S13. Islet health in a retrieved iBEDv1 at 2 months from a mouse with well-controlled BG. Microscope images of (A) H&E staining and (B) nuclei (DAPI; blue)/CD3 (T cell marker; red) staining of the device-host boundary show no signs of inflammation and rare, sporadic CD3+ cells (T cells). (C) H&E staining and (D) nuclei (DAPI; blue)/insulin (red) immunostaining of islets in regions far away from the tank indicating a few partially unhealthy cells.

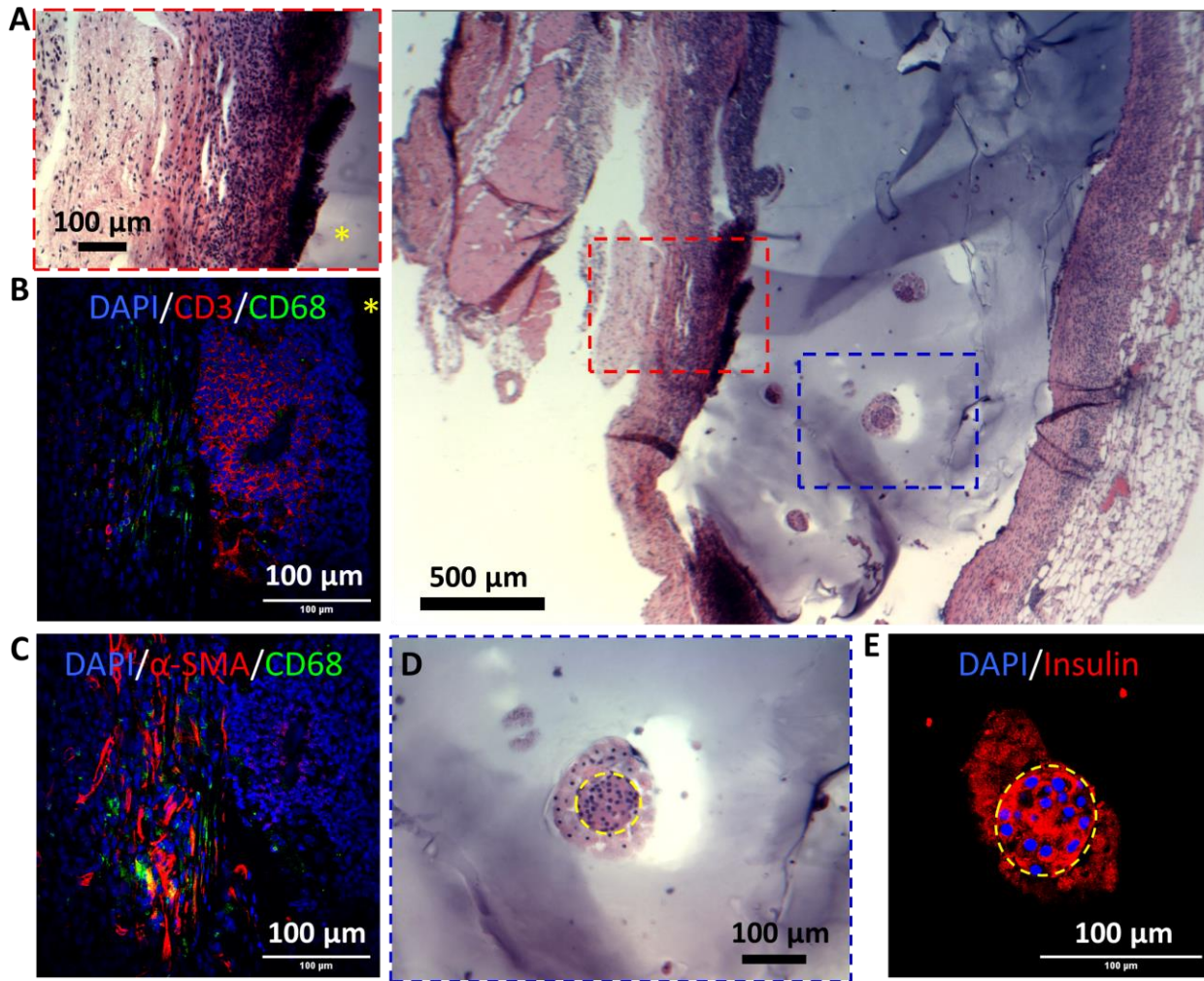


Fig. S14. Islet health in a retrieved iBEDv1 at 2 months from a mouse with poorly controlled BG. (A) H&E staining of the fibrotic tissue surrounding the implanted iBEDv1 showing a vigorous inflammatory response, a layer of dense immune cells located at the device-host boundary. (B) nuclei (DAPI; blue)/CD3 (T cell marker; red)/CD68 (macrophage marker; green) staining showing mass accumulation of CD3 positive T cells at the boundary (asterisk indicates the device side of the device-host boundary) and moderate macrophage accumulation in fibrotic tissue several cell layers away from the boundary. (C) DAPI/CD68/ α -SMA (myofibroblasts, red) staining, showing myofibroblasts and macrophages in fibrotic tissue several cell layers away from the boundary, few myofibroblasts and macrophage near the interface. (D) H&E staining and (E) DAPI/insulin (red) staining of a select islet, showing functional core cells, but unhealthy and non-functional peripheral cells.

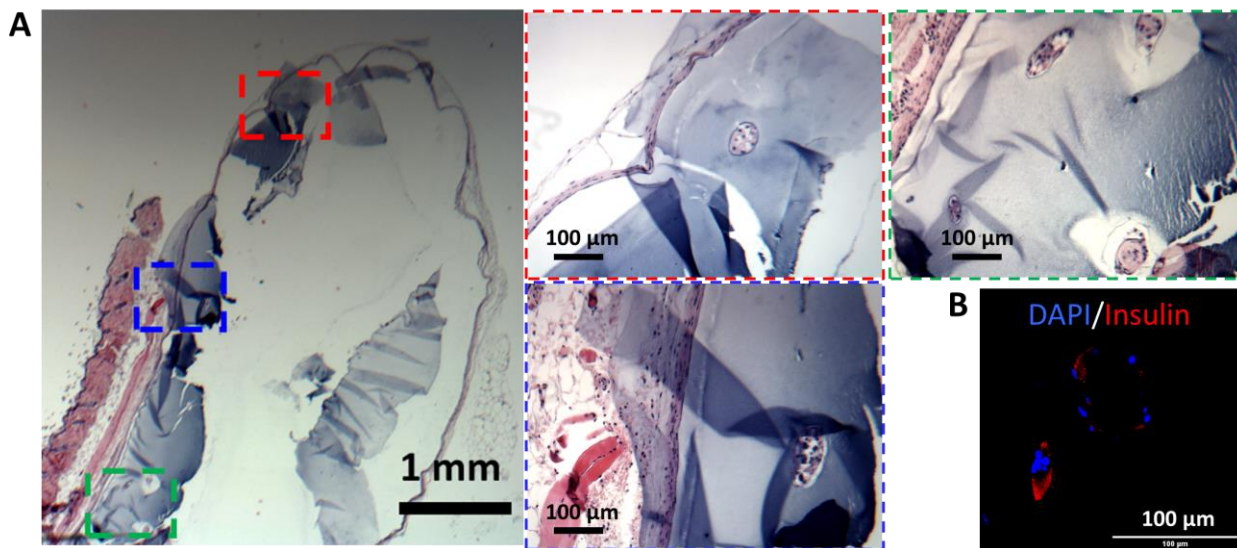
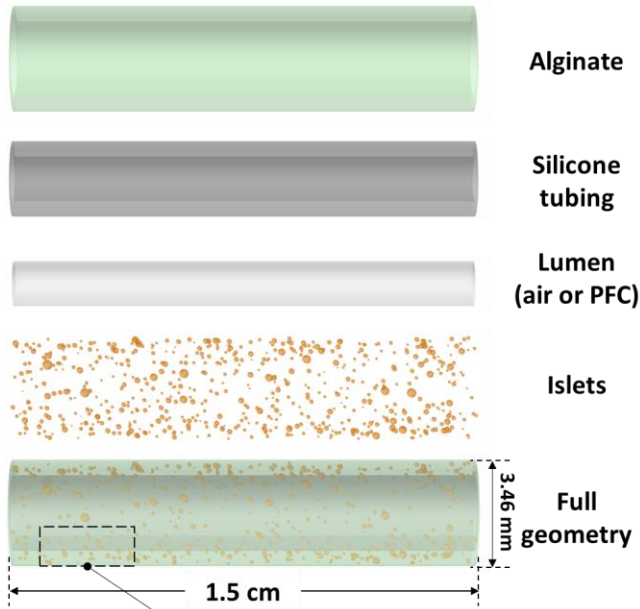


Fig. S15. Islet health in a retrieved control device (*i.e.* a device similar to iBEDv1 but without the inverse-breathing feature) at 2 months from a mouse. Microscope images of (A) H&E staining of a retrieved control sample showing several necrosed islets with severe karyorrhexis or complete loss of nuclei. (B) Nuclei (DAPI; blue)/insulin (red) immunostaining showing weak positive signals for both markers; no DAPI signal was observed in the necrotic core, and only few insulin positive cells were detected in peripheries.

A Control, iBEDv1, iBEDv2 components



iBEDv3 components

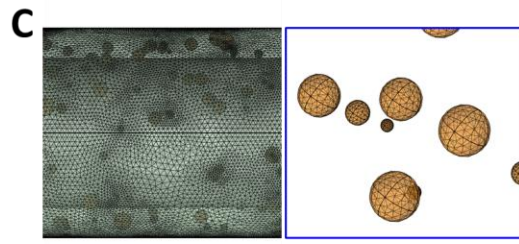
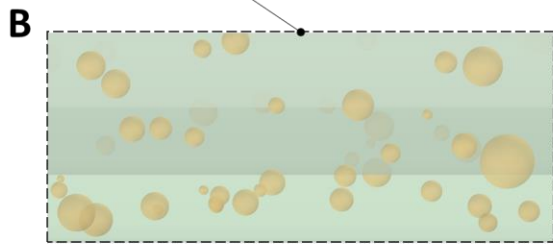
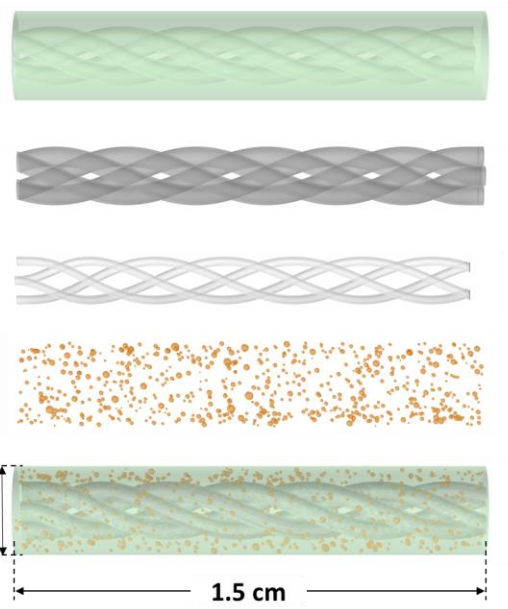


Fig. S16. Computational model development. (A) Schematics illustrating components of the control, iBEDv1, and iBEDv2 designs (left column) and iBEDv3 design (right column) including the alginate, silicone tubing, tubing lumen (air for control, iBEDv2, iBEDv3 designs, PFC for iBEDv1 design), and randomly distributed islets. (B) A high magnification image showing the randomly distributed islets in the alginate. (C) An image showing the nonuniform mesh on the alginate surface (left) and on individual simulated islets (right). (D) An annotated schematic showing the dimensions for each design.

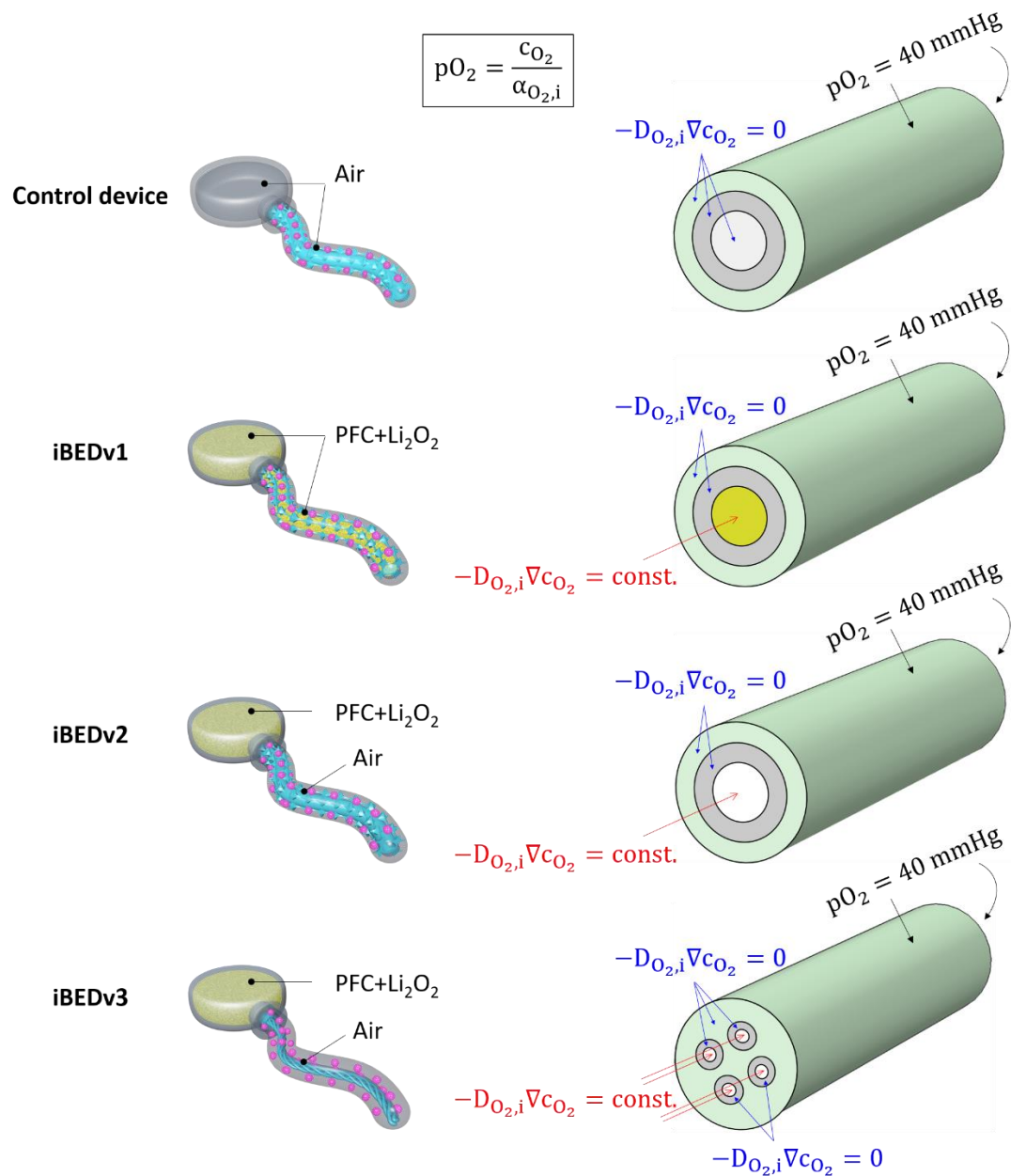


Fig. S17. Model boundary conditions. Schematic representation of model-implemented boundary conditions in the (top to bottom) control device, iBEDv1, iBEDv2, and iBEDv3. In all designs, boundary pO_2 was a constant of 40 mmHg along the length of the alginate cylinder and at the face representing the device end, the combination of which represented the device-host interface. In the control design, a no-flux condition (blue) was implemented on all surfaces representing the tank-cylinder interface. In iBEDv1, iBEDv2, and iBEDv3 designs, O_2 generation from the tank was implemented as a constant surface flux (red) on the surface of the tubing lumen(s). No flux conditions were implemented on the tank-silicone and tank-alginate interfaces on this face in all designs. Concentration of oxygen (c_{O_2}) was converted into pO_2 by the relationship shown in the boxed equation.

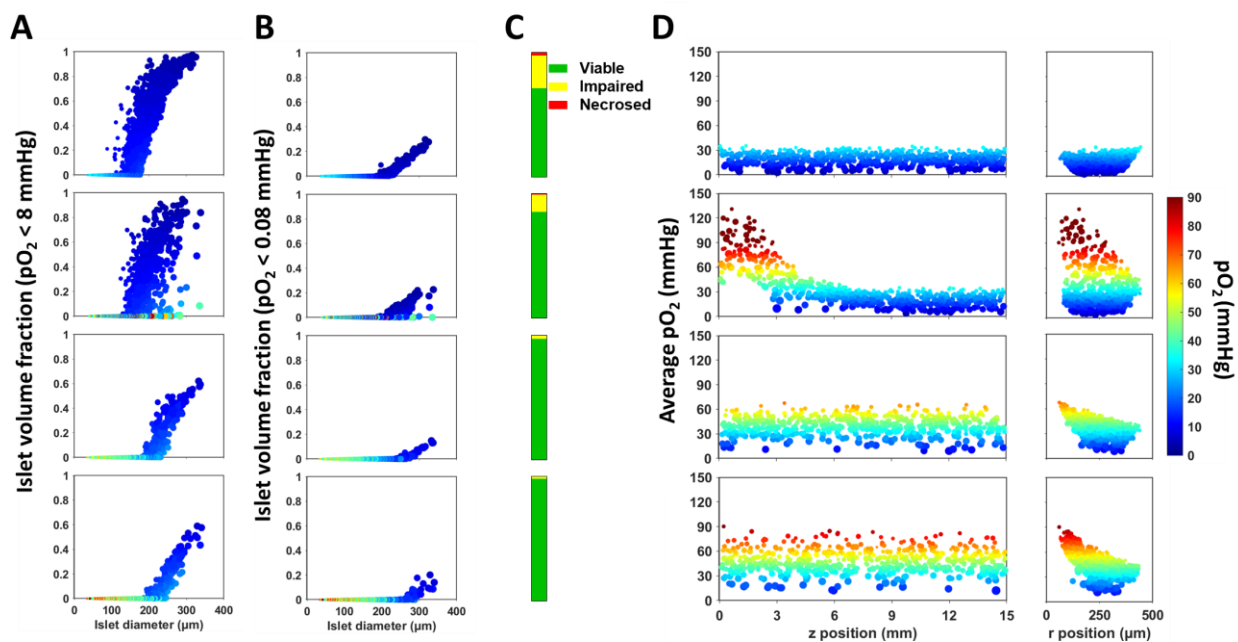


Fig. S18. Simulation-predicted islet oxygenation. (A to D) Islet survival and oxygenation in (top to bottom) the control device, iBEDv1, iBEDv2, and iBEDv3 from one iteration selected at random; each point represents a simulated islet. Scatter plots of islet diameter versus predicted individual islet volume fraction of (A) metabolically unresponsive ($pO_2 < 8$ mmHg) tissue and (B) necrotic ($pO_2 < 0.08$ mmHg) tissue. (C) Predicted net volume fraction of necrotic tissue (red), metabolically unresponsive tissue (yellow) and functional tissue ($pO_2 > 8$ mmHg). (D) Scatter plots of islet diameter versus predicted oxygenation according to z position (left column) and radial position (right column) from a single iteration.

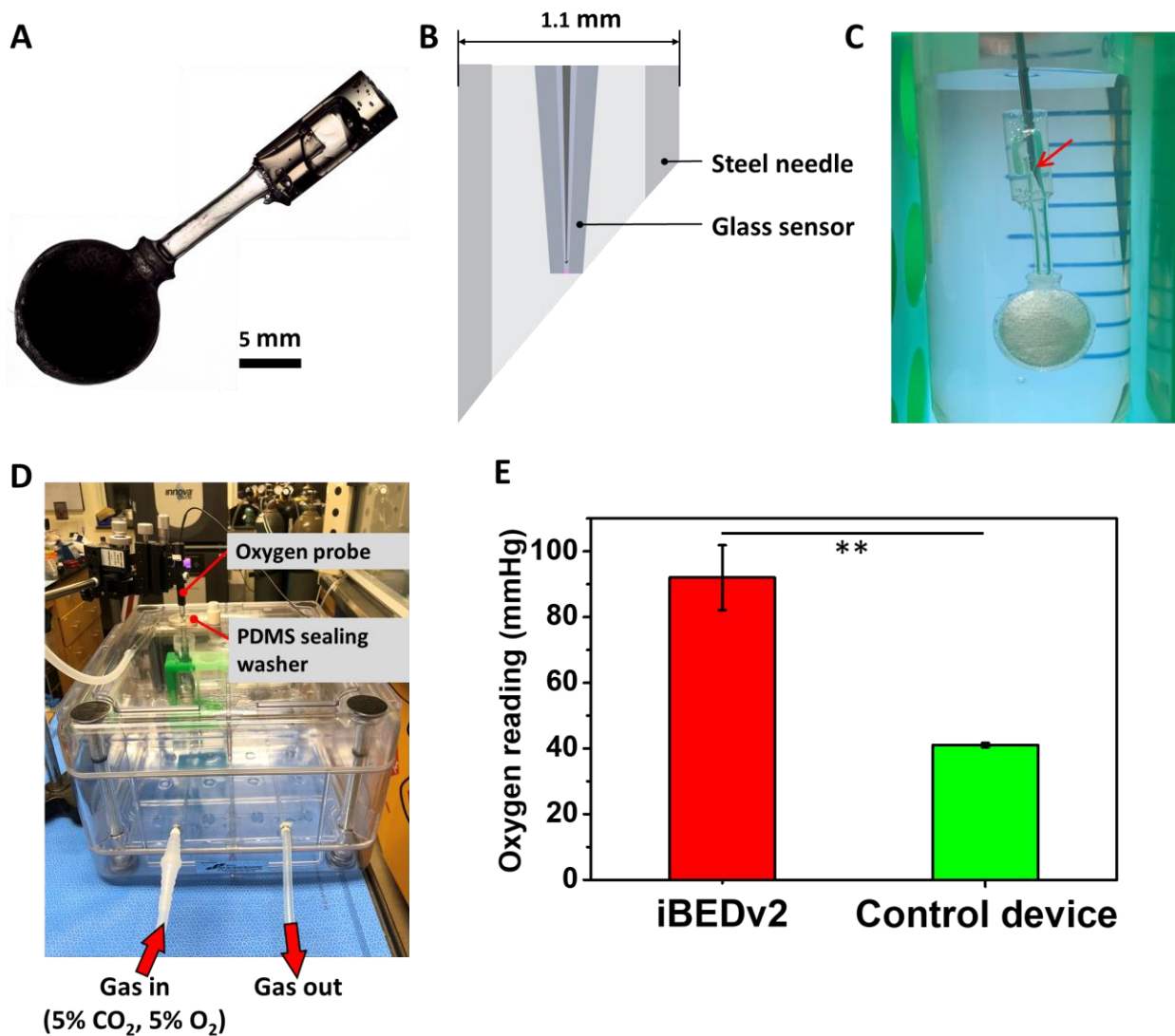


Fig. S19. pO₂ measurement in the lumen of iBEDv2 and the corresponding control device. (A) Stereo microscope image of the iBEDv2 adapted for lumen pO₂ measurement. (B) Schematic representation of the O₂ needle sensor used for measurement. (C) Digital image of the measurement test: the device was submerged in a buffer equilibrated to 5 CO₂, 5% O₂; the O₂ microsensor was then inserted through the PDMS attachment and into the (gas phase) lumen of the silicone tubing to obtain a measurement (red arrow indicates microsensor tip inserted in the measurement adapter); the test was performed in a closed gas chamber (D) supplied with a continuous gas (5% CO₂, 5% O₂) flow. (E) Measured lumen pO₂ in iBEDv2 (n = 2) and control devices (n = 3) (***p* < 0.01). We note that the device was immersed saline in a 50 mL Falcon tube and incubated in a hypoxia incubator with 5% CO₂, 5% O₂ for two weeks before the measurements. Measurements were taken at the end of this two-week period. The Falcon tube was sealed before being taken out from the hypoxia incubator and transferred into a sealed and pre-equilibrated hypoxia chamber to conduct the oxygen measurement. The closed hypoxia chamber was supplied with a continuous gas flow (5% CO₂, 5% O₂, 90% N₂) from a gas cylinder. Then, the oxygen probe was introduced into the chamber from a top window and sealed with a PDMS washer. After checking that the oxygen condition was equilibrated to 5% O₂ inside the chamber, the oxygen probe was insert into the device lumen for the final measurement. Photo credits (C and D): Long-Hai Wang, Cornell University.

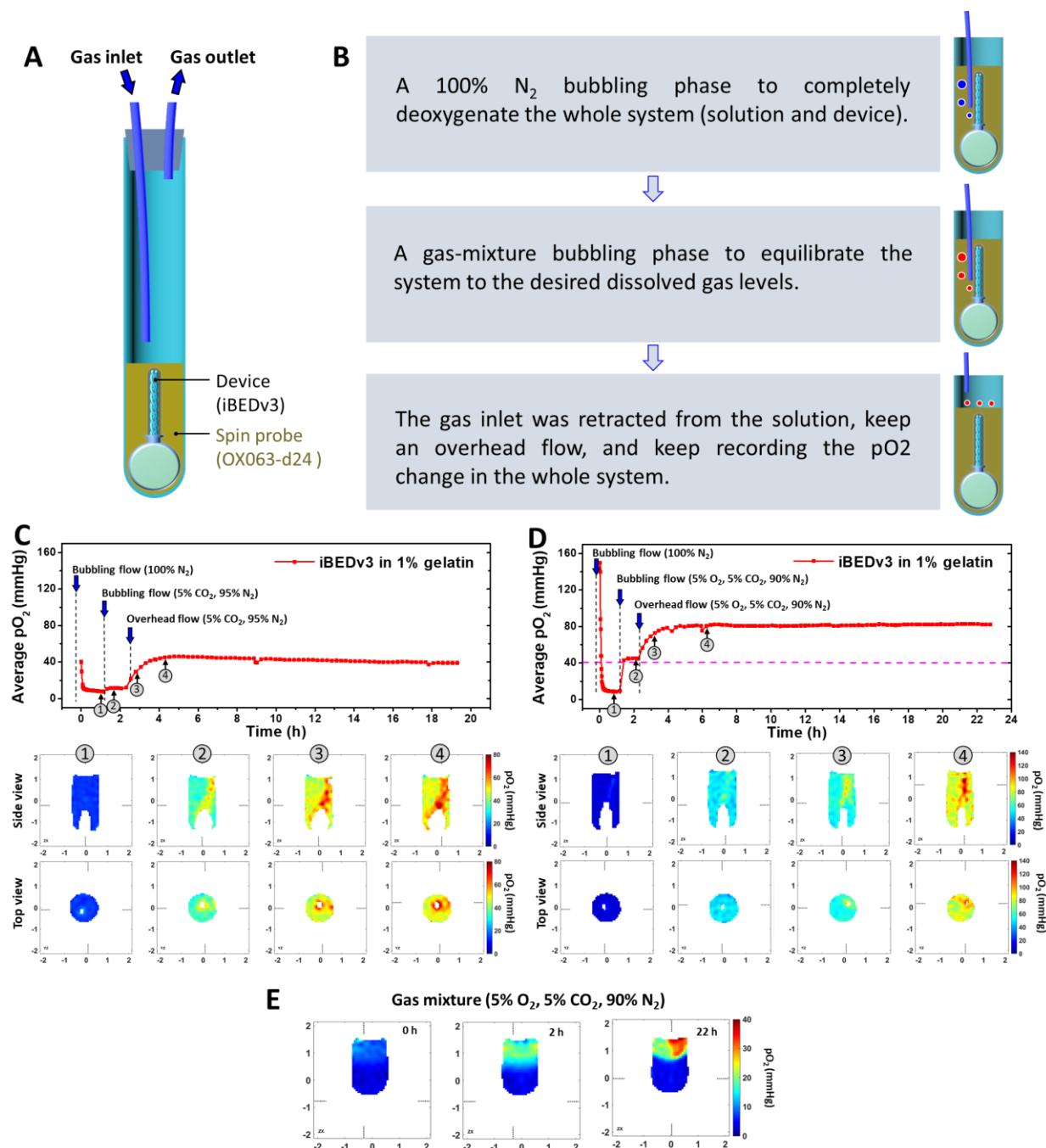


Fig. S20. EPR O₂ imaging. (A) Schematic showing the container for the pO₂ distribution mapping study: the device was placed in spin probe solution within a sealed glass vial; a gas inlet was used for sample aeration, and a gas outlet was included for venting. (B) An abbreviated aeration protocol used in the EPR O₂ imaging studies. Average pO₂ measurements in the whole system (*i.e.* solution and device) versus time and cross-section pO₂ distributions on two planes (side view and top view) at four times (indicated by the arrows in the time series plots) in an iBEDv3 in 1% gelatin subjected to a gas mixture of (C) 5% CO₂, 95% N₂ and (D) 5% CO₂, 5% O₂, 90% N₂. (E) Cross-section pO₂ distribution in 1% gelatin (no device) subjected to overhead flow with 5% CO₂, 5% O₂, 90% N₂ (no bubbling phase after deoxygenation), showing poor penetration of O₂ over time.

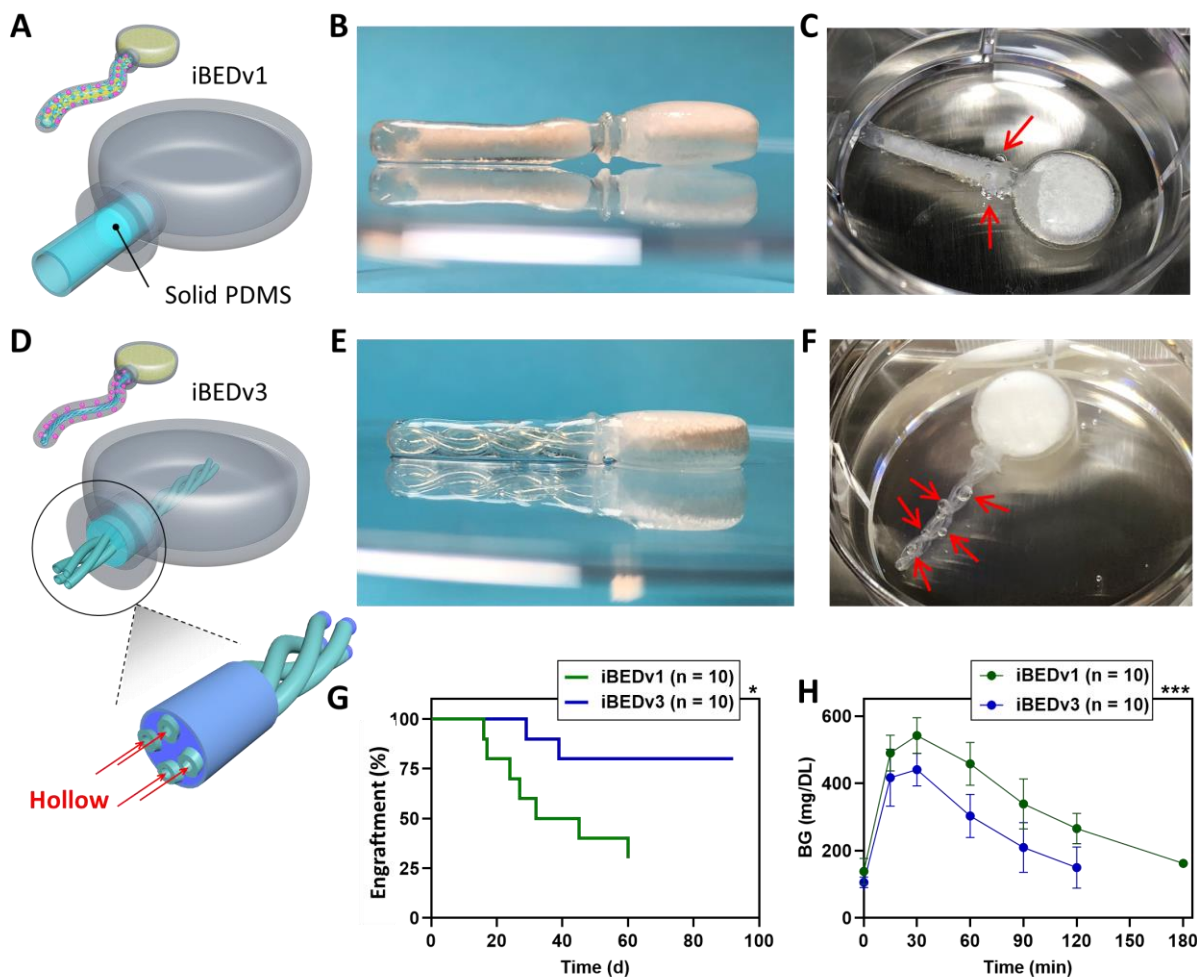


Fig. S21. Design improvements in iBEDv3. (A) Schematic of the iBEDv1 device, highlighting the PDMS adapter connecting the terminal tank to the silicone tubing. This required slow CO₂ and O₂ transport in the solid phase (through the PDMS adapter) and the liquid phase (through the PFC in the lumen). (B) Digital image of an iBEDv1 retrieved at 2 months from a mouse, showing tank inflation due to positive pressure from gas build-up in the terminal tank. (C) Digital image of the retrieved iBEDv1 following incubation in 5% CO₂, 5% O₂, showing bubble formation only near the terminal tank (red arrows indicate bubbles). (D) Schematic of the iBEDv3, highlighting the PDMS adapter penetrated by the twisted hollow silicone tubing, allowing rapid CO₂ and O₂ transfer in the gas phase. (E) Digital image of a retrieved iBEDv3 at 3 months from a mouse, showing the absence of tank inflation. (F) Digital image of the iBEDv3 device following incubation in 5% CO₂, 5% O₂, showing consistent bubble formation both near and far from the terminal tank (red arrows indicate bubbles). (G and H) Comparison of therapeutic function of iBEDv1 and iBEDv3 in mice. (G) Engraftment percent of the iBEDv1 and iBEDv3 summarized from the pulled BG data of *in vivo* studies (Fig 3e and 6j) (Mantel-Cox, **p* < 0.05). Device “failure” was defined as 3 consecutive readings over 250 mg/dL. (H) IPGTT data pulled from the iBEDv1 and iBEDv3 *in vivo* studies (Fig 3f and 6k) (two-way ANOVA, ****p* < 0.001). Photo credits (B, C, E, and F): Long-Hai Wang, Cornell University.

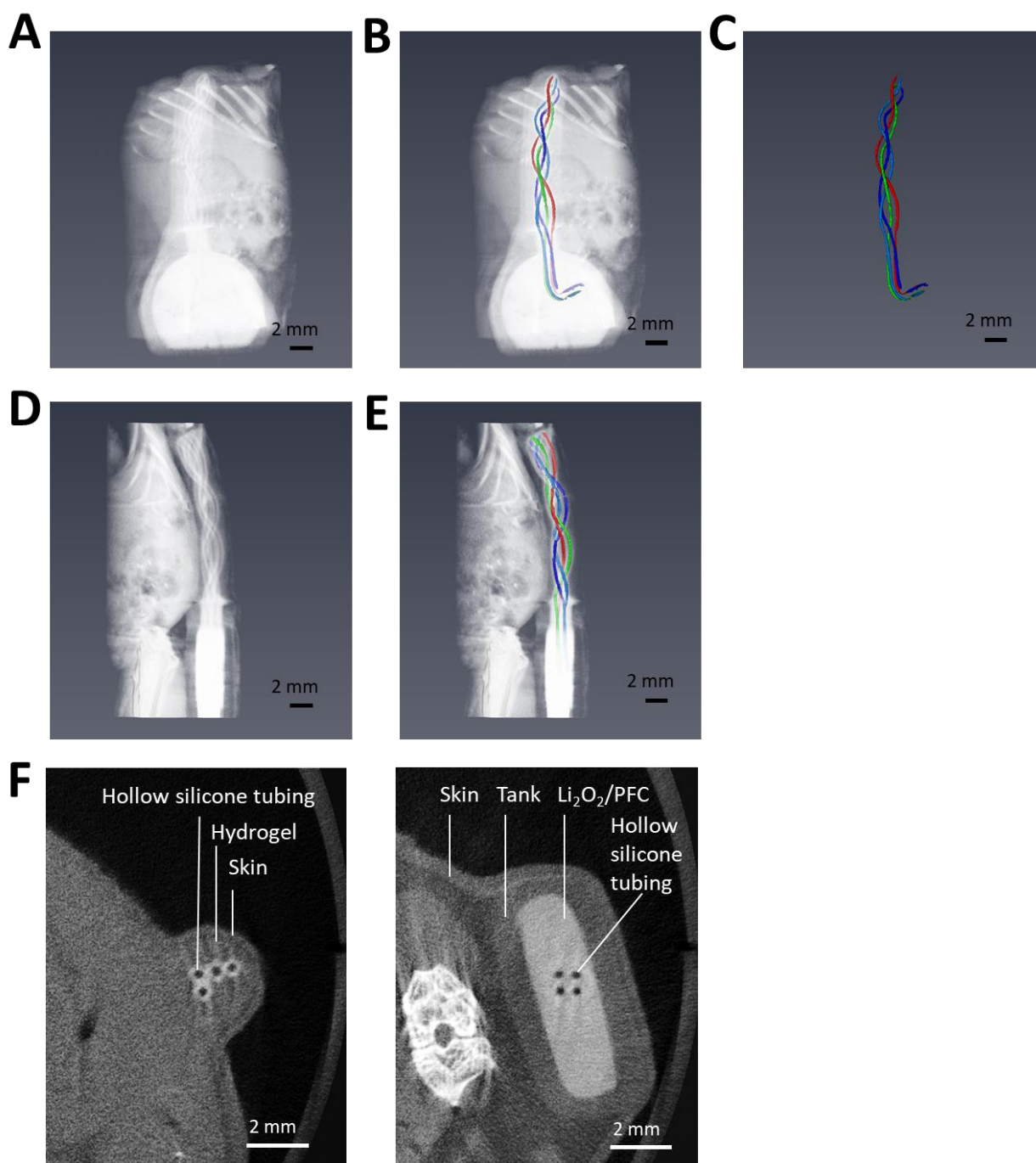


Fig. S22. Micro-CT scans of the iBEDv3 device implanted in a mouse for 3 months. (A to E) 3D reconstruction of micro-CT images of an iBEDv3 in a mouse. (A and B) Top and (D and E) side views of the implanted device in a mouse. An intensity threshold was applied to the images, isolating the lumens of the twisted silicone tubing, suggesting that a gas phase was maintained (note: four different colors, one for each lumen, were applied retroactively). The isolated lumens of the twisted tubing are shown in (C). (F) Two transverse 2D cross-sections of the iBEDv3 in a mouse, illustrating the preserved hollow structure of the silicone tubing both within the encapsulation domain (left) and the tank (right).

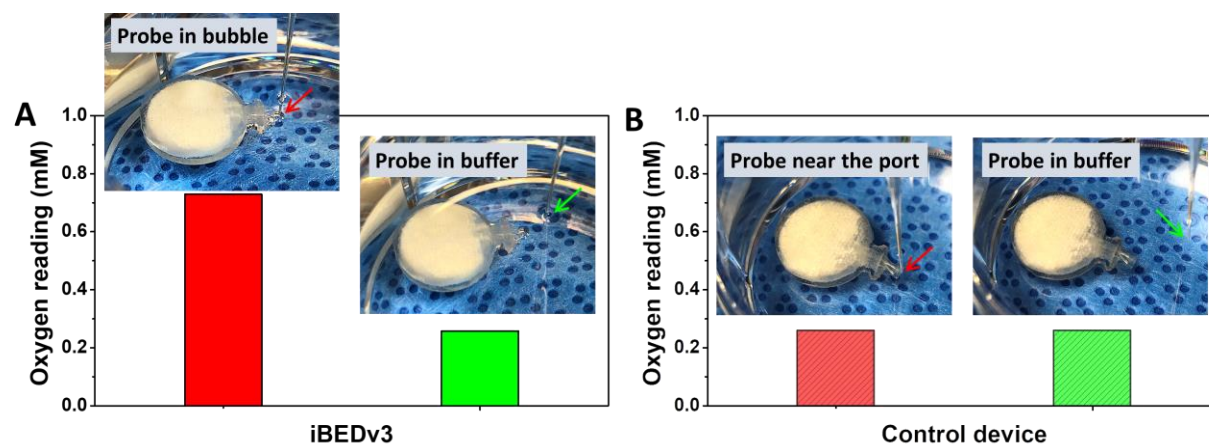


Fig. S23. Maintained CO₂-responsive O₂ production in an iBEDv3 retrieved from a mouse at 3 months. (A) An iBEDv3 device, retrieved from mice at 92 d, was truncated at the PDMS adapter and incubated in 5% CO₂, 20% O₂. O₂ content was measured in the bubbles forming at the PDMS adapter-buffer interface (the twisted silicone tubing of iBEDv3 was cut), and in the bulk buffer, indicating maintained CO₂-responsive O₂ production at this time point. Arrows indicate the O₂ microsensor tip. (B) Similar measurements performed on a retrieved control device showed near the equilibrium level (~0.25 mM, 20% O₂) in measurements of the probe near the tank port and in the buffer. Arrows indicate the O₂ microsensor tip. Photo credits (A and B): Long-Hai Wang, Cornell University.

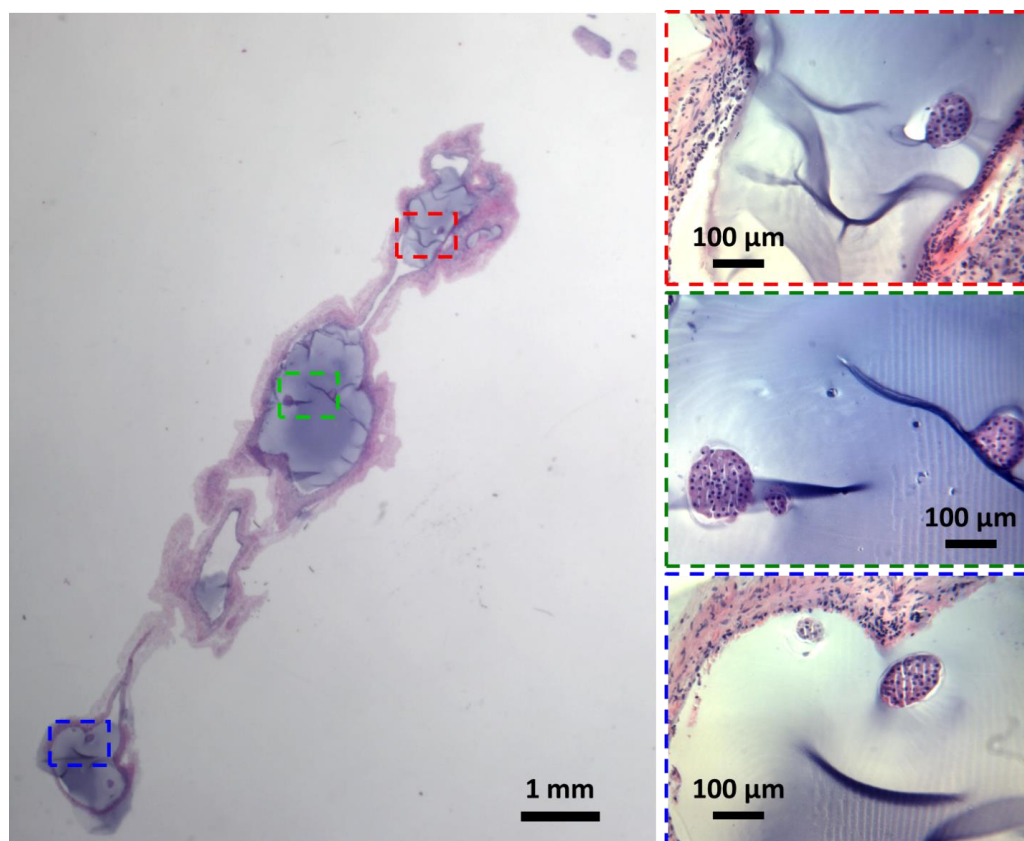


Fig. S24. Islet health in an iBEDv3 and surrounding fibrotic tissue retrieved from a mouse at 3 months. H&E staining of a superficial section of alginate with surrounding fibrotic tissue in an iBEDv3. High magnification images (right panel) showing several healthy islets at locations proximate, intermediate, and distal to the tank.

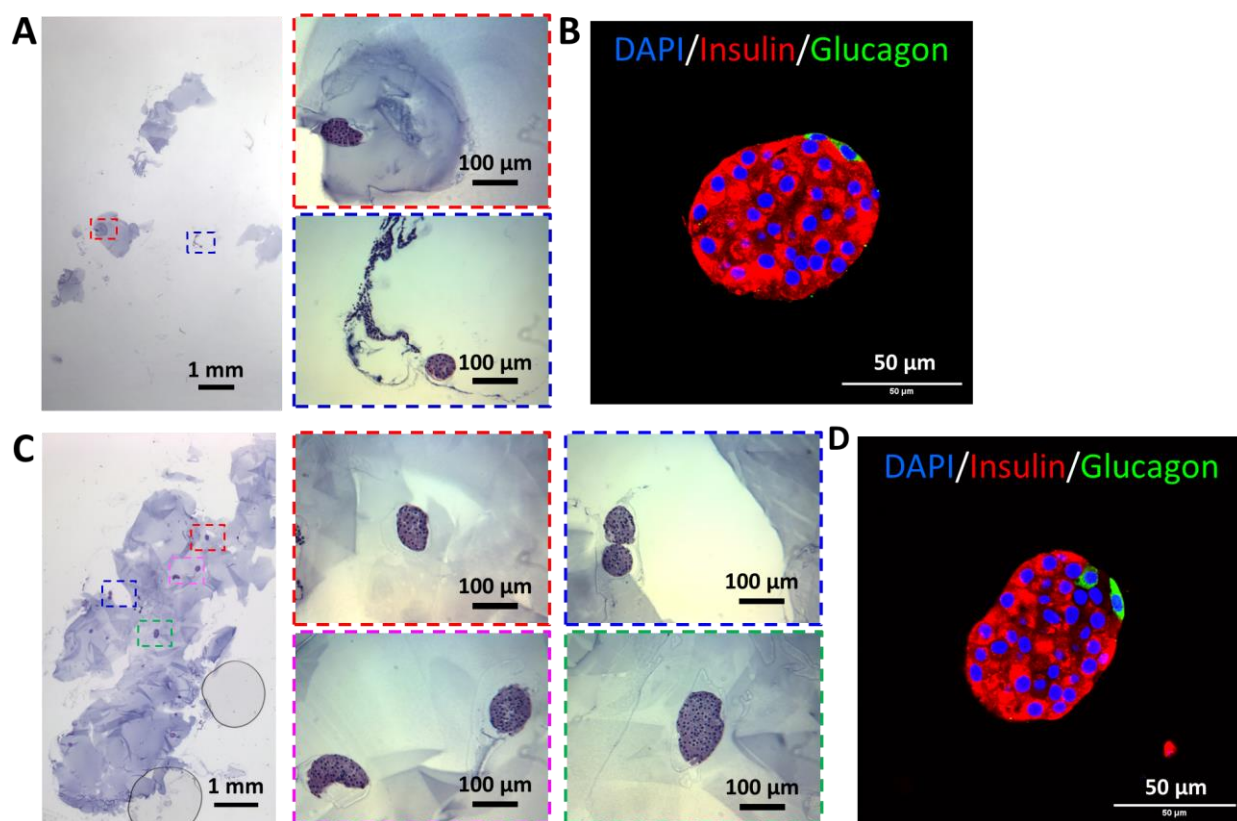


Fig. S25. Islet health in an iBEDv3 retrieved from a mouse at 3 months. H&E and nuclei (DAPI; blue)/insulin (red)/glucagon (green) immunostaining of a superficial section (A and B) and a deeper section (C and D) of alginate in an iBEDv3. Numerous healthy and insulin/glucagon positive islets were found in both sections. Note: the fibrotic capsule was removed during retrieval.

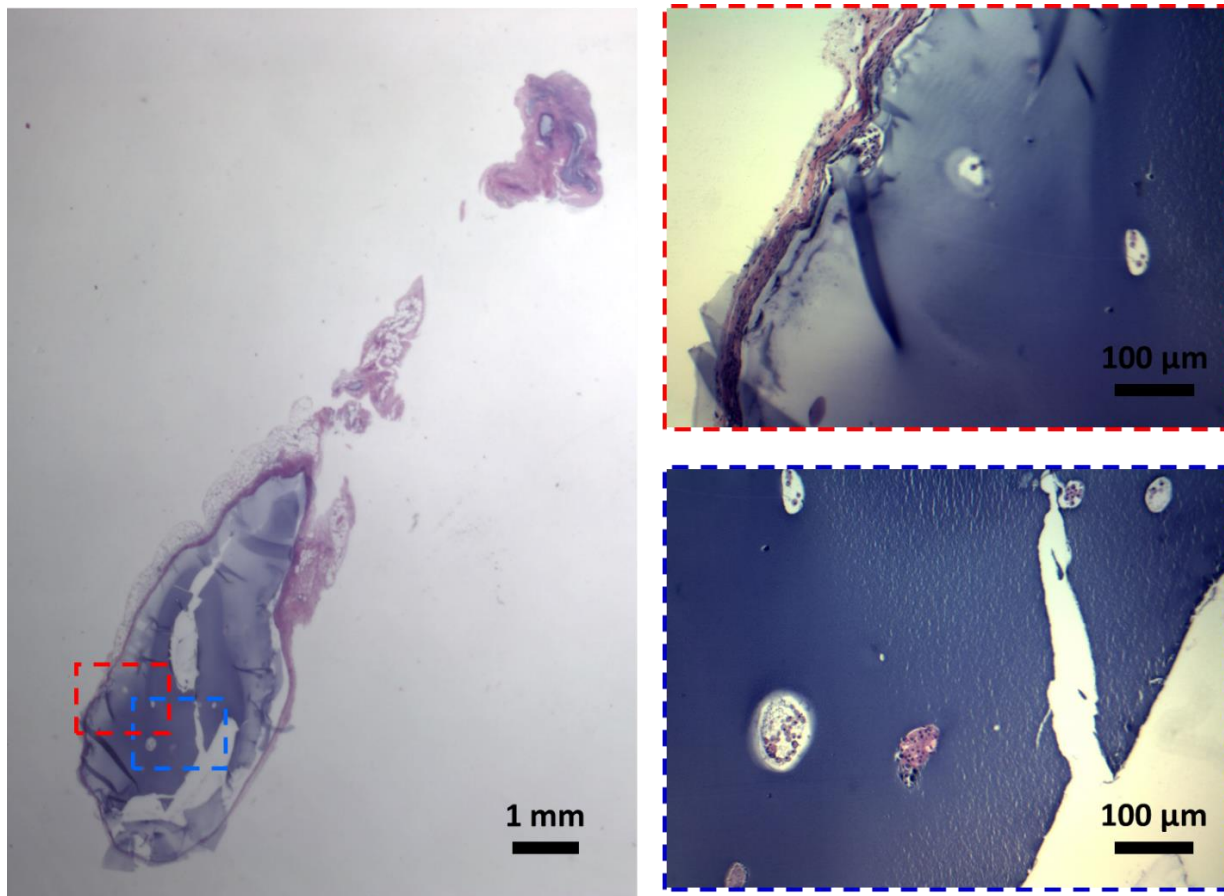


Fig. S26. Islet health in a control device (*i.e.* a device similar to iBEDv3 but without the inverse-breathing feature) retrieved from a mouse at 3 months. H&E staining of a superficial section of a retrieved control iBEDv3 sample. Most observed islets were necrosed.

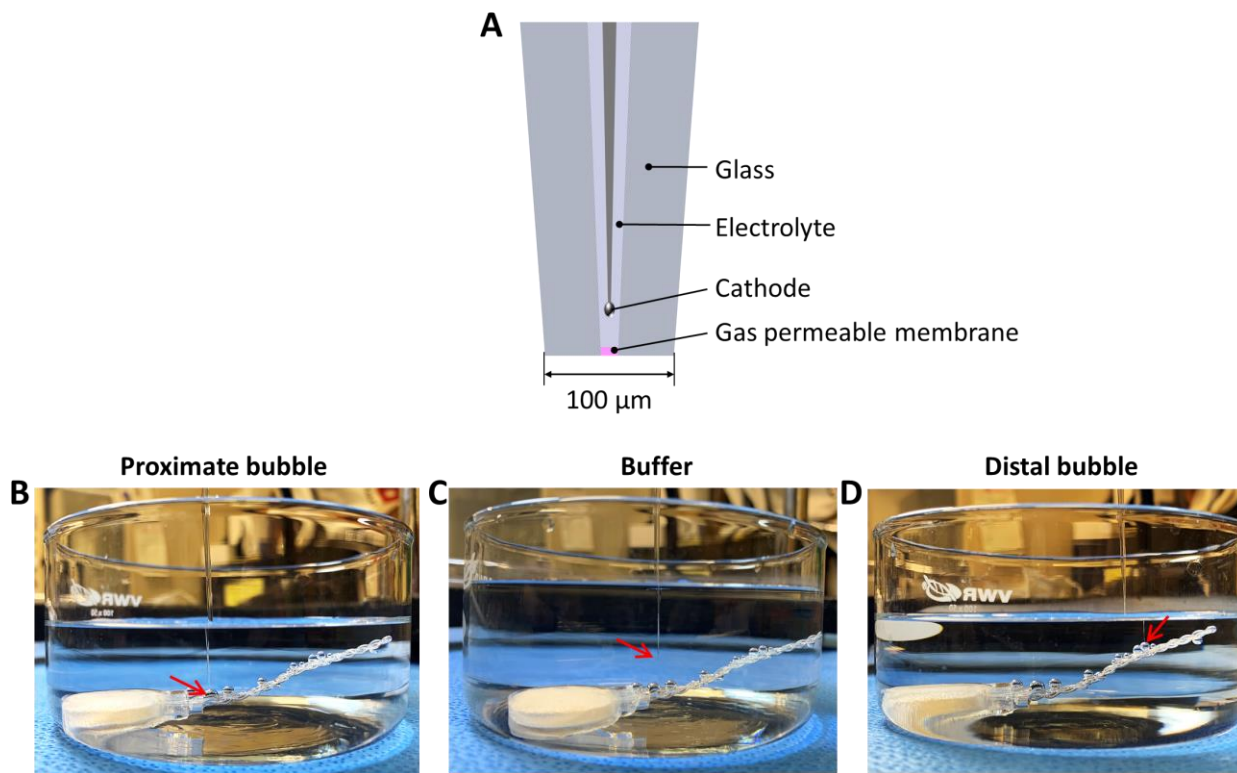


Fig. S27. Microsensor O_2 measurements in an iBEDv3S for pig transplantation. (A) Schematic showing the components of the O_2 microsensor (OX-100, Unisense) used for direct measurement. O_2 measurements in (B) a bubble proximate to the terminal tank, (C) the buffer, and (D) a bubble distal to the terminal tank following incubation in 5% CO_2 , 20% O_2 . Arrows indicate the microsensor tip. Photo credits (B to D): Long-Hai Wang, Cornell University.

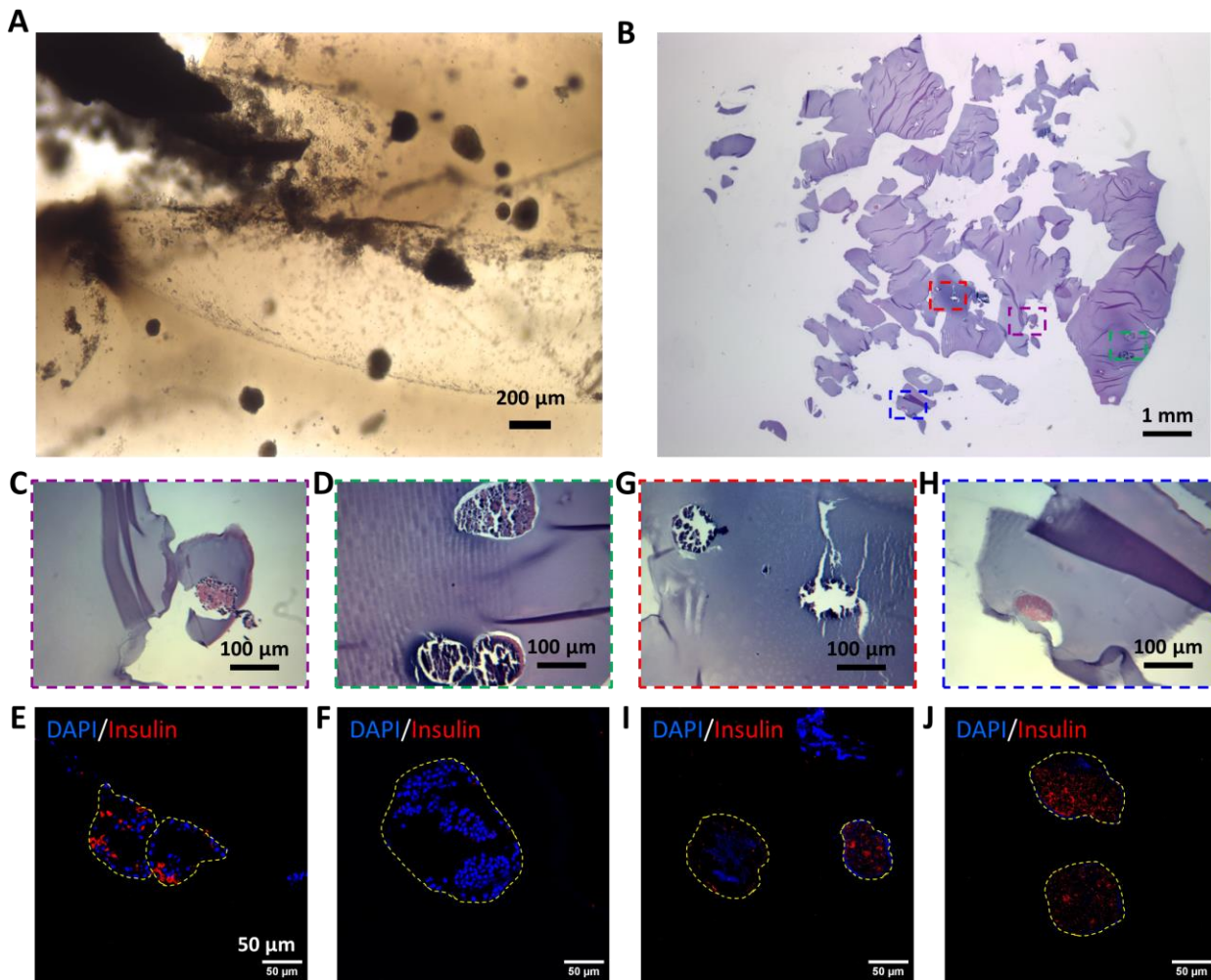


Fig. S28. Viability of rat islets from a control device (*i.e.* a device similar to iBEDv3S but without the inverse-breathing feature) retrieved at 1 month following SC implantation in a Göttingen minipig. (A) Stereo microscope image of a region of hydrogel from the retrieved sample; islets were all dark, with a rough surface. **(B)** H&E staining of the collected hydrogel from the retrieved device. No healthy islets were found in the whole section. **(C and D)** H&E staining and **(E and F)** nuclei (DAPI; blue)/insulin (red) immunostaining showing some necrosed islets with severe karyorrhexis; fragmented nuclei and sporadic insulin positive cells were detected. **(G and H)** H&E staining and **(I and J)** nuclei/insulin immunostaining showing some necrosed islets with complete loss of nuclei, faint DAPI signal in the islets remains.

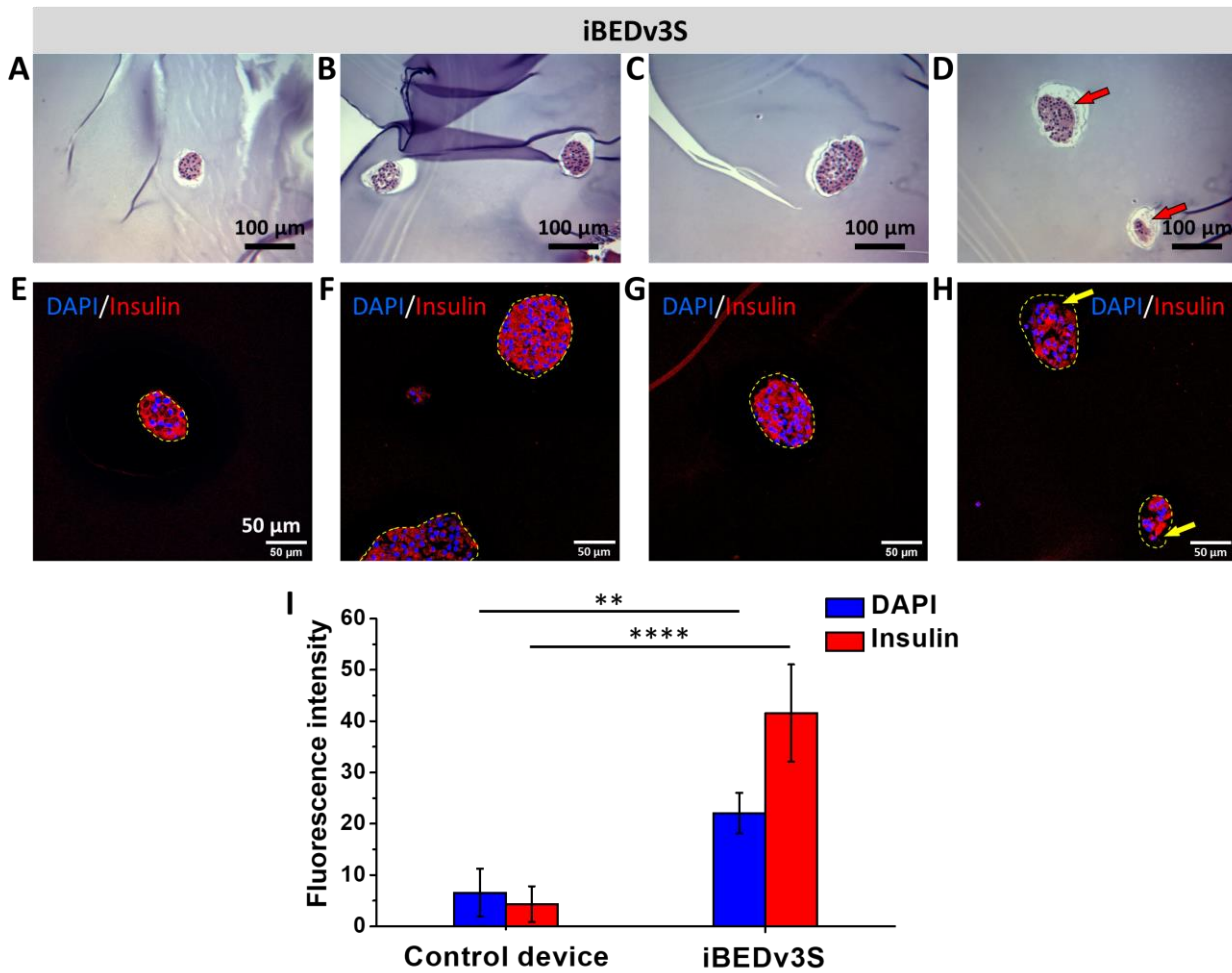


Fig. S29. H&E staining of one rat islet encapsulation iBEDv3S retrieved at 1 month following SC implantation in a Göttingen minipig. (A to H) Numerous healthy islets were observed in the retrieved device (Fig. 7g), though some cells in islet peripheries were found to be apoptotic in a few islets (arrows in D and H), likely due to xenogeneic immunological response rather than hypoxia, which usually causes necrosis in the islet center. (I) Comparison of islet function in this iBEDv3S (E to H) and the control device in above Fig. S28 (E, F, I, and J)) by quantification of insulin and DAPI fluorescence intensity of the stained islets to evaluate the islet functionality and karyorrhexis (fragmented nuclei)/loss of nuclei in islets, respectively. Specially, insulin expression was 9.6-fold higher (two-way ANOVA followed by Tukey's post-hoc p -value adjustment, **** $p < 0.0001$) and DAPI content was 3.4-fold higher (two-way ANOVA followed by Tukey's post-hoc p -value adjustment, ** $p < 0.01$) in islets from iBEDv3S compared to islets from control device, quantitatively confirming that the iBEDv3S yielded substantial improvements in islet survival and function in pigs.

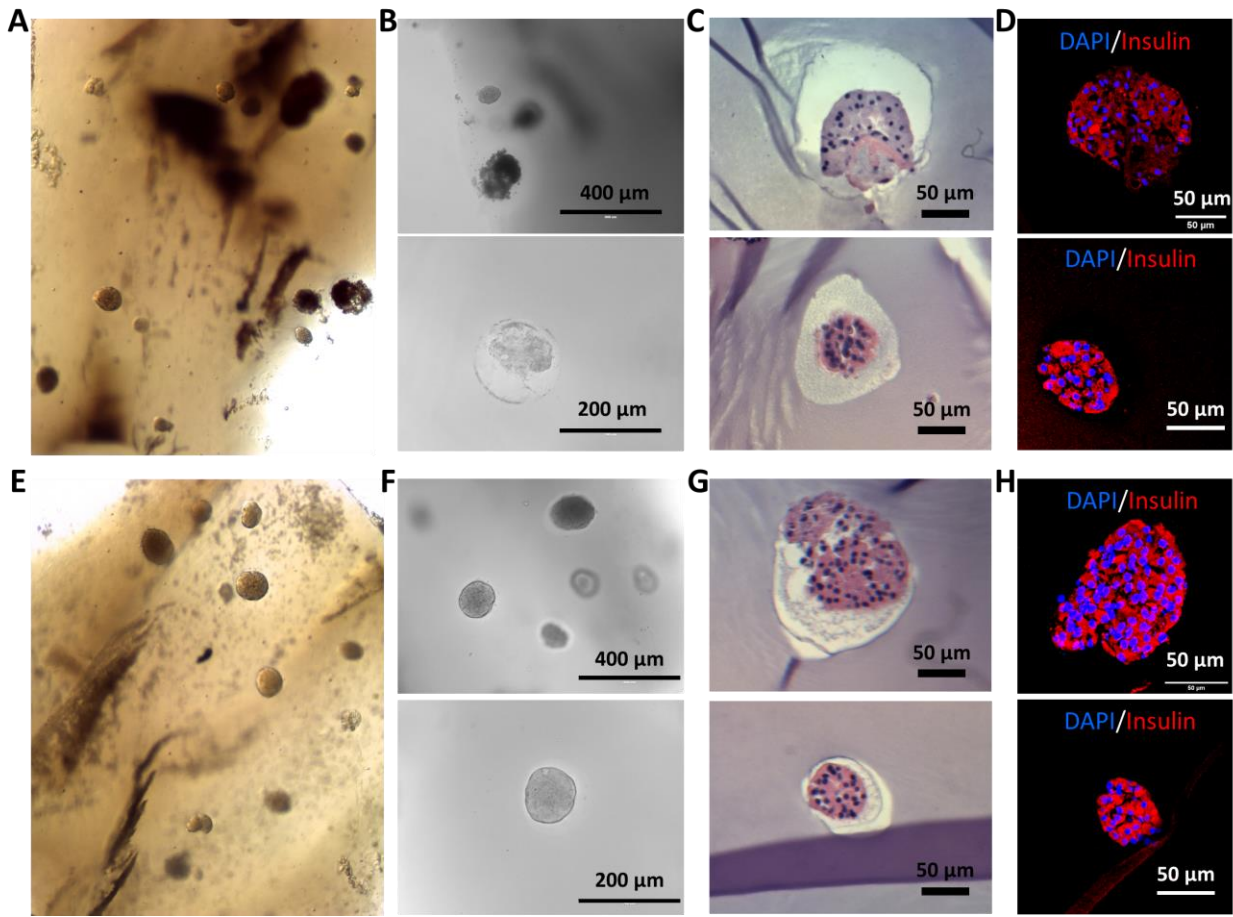


Fig. S30. Islet viability in one rat islet encapsulation iBEDv3S retrieved at 2 months following SC implantation in a Göttingen minipig. (A) Stereo microscope image and (B) bright-field microscope images showing a region of hydrogel from the retrieved sample; some healthy islets appeared as yellow and maintained a smooth and intact morphology, and some unhealthy islets showed as dark, and presented a rough surface and loose morphology. (C) H&E staining and (D) nuclei (DAPI; blue)/insulin (red) immunostaining of some islets with partially unhealthy cells. (E) Stereo microscope image and (F) bright-field microscope images showing a region of hydrogel from the retrieved sample; most islets were healthy, appearing as yellow with maintained smooth and intact morphology. (G) H&E staining and (H) nuclei/insulin immunostaining of select healthy islets.

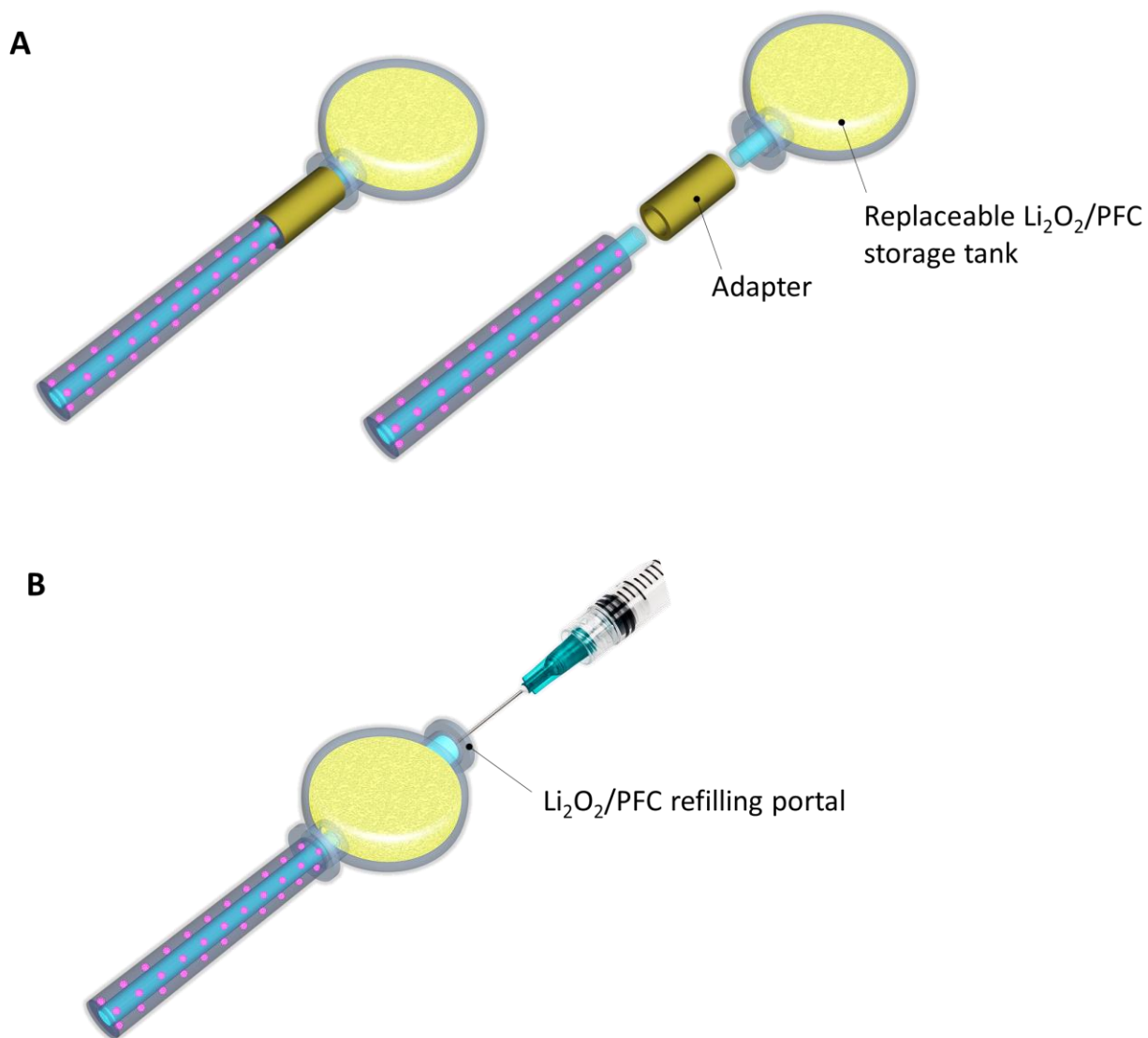


Fig. S31. Prospective designs extending the lifetime of O_2 supply indefinitely. Schematics showing (A) a potential modular design for a tank that can be replaced and (B) a design which features a portal in the terminal tank through which the expired $\text{Li}_2\text{O}_2/\text{PFC}$ can be withdrawn and refilled.

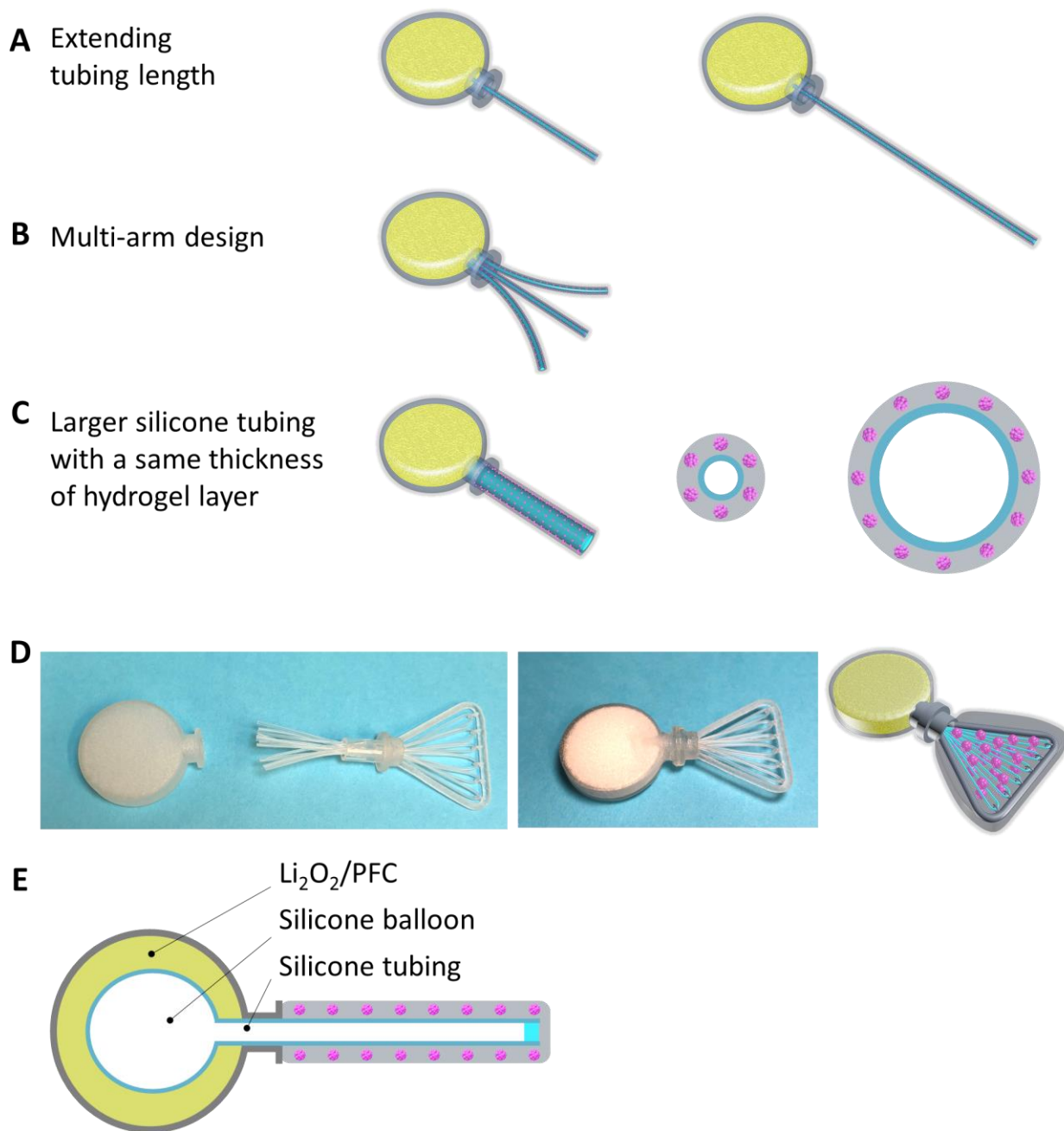


Fig. S32. Prospective designs to increase capacity. (A to C) Schematics showing designs which increase the volume of transplantable islets including (A) extending length of the cell encapsulation tubing, (B) implementing multiple parallel cell encapsulation domains connected to a single tank, and (C) expanding the diameter of the inner of the tank. (D) Digital images (left, middle) and a schematic showing a design for a planar device prototype with multiple aeration channels connected to the terminal tank to increase islet capacity. (E) A schematic showing a design to improve the O_2 delivery rate to support higher islet densities, by introduction of a silicone balloon in the terminal tank. Photo credit (D): Long-Hai Wang, Cornell University.

Table S1. O₂ content of Li₂O₂ compared to O₂ demand of rat and human islets. In the inverse-breathing reaction, 1 mg of Li₂O₂ yields 0.348 mg O₂. Considering the maximum O₂ consumption rate of rat islets, 50 mg of Li₂O₂ should support 500 IEQ rat islets for 210 d, assuming all O₂ is consumed by the cells. Under this assumption, and considering the O₂ consumption rate of human islets, 3 g Li₂O₂ should support 500 k IEQ human islets for 33 d. Note, this comparison does not consider physical transport phenomena such as diffusion, leakage, and O₂ supply from the host.

$2\text{Li}_2\text{O}_2 + 2\text{CO}_2 \rightarrow 2\text{Li}_2\text{CO}_3 + \text{O}_2$		Rat islets	50 mg Li ₂ O ₂	Human islets	3 g Li ₂ O ₂
Li ₂ O ₂	O ₂	Maximum oxygen consumption rate	500 IEQ rat islets	Maximum oxygen consumption rate	500 k IEQ human islets
1 mg 0.0218 mmol	0.348 mg 0.0109 mmol	0.034 mol/m ³ /s 6.01 E-14 mol/IEQ/s	210 days	0.013 mol/m ³ /s 2.3 E-14 mol/IEQ/s	33 days

Video S1: A liquid perfusion study showing hollow structure of the twisted silicone tubing.

Video S2: A gas perfusion study showing the gas-permeability of the silicone tubing.

Video S3: Subcutaneous implantation of an iBEDv3S in a Göttingen minipig.